Transient elastohydrodynamic analysis of rough surfaces using a novel coupled differential deflection method

C. D. Elcoate, H. P. Evans, T. G. Hughes and R. W. Snidle

Proceedings of the Institution of Mechanical Engineers, Part J: Journal of Engineering Tribology 2001 215: 319
DOI: 10.1243/1350650011543574

Transient elastohydrodynamic analysis of rough surfaces using a novel coupled differential deflection method

C D Elcoate, H P Evans*, T G Hughes and **R W Snidle**
Mechanical Engineering and Energy Studies Division, Cardiff School of Engineering, Cardiff University, Wales, UK

Abstract: The paper presents a transient analysis technique for line contact elastohydrodynamic lubrication problems using coupled elastic and hydrodynamic equations. Full coupling is made possible by use of a novel differential deflection formulation. The lubricant is treated as non-Newtonian with a non-linear Eyring-type relationship between shear stress and shear strain rate. Results are presented for moving rough surfaces where the roughness data are taken from profilometer traces of run-in ground surfaces. A complete range of slide–roll ratios has been considered and results are shown for one rough surface in rolling/sliding motion against a smooth surface with extremely low lambda ratios (ratio of minimum film clearance to r.m.s. roughness). Results are also shown for two rough surfaces in contact under severe thin-film high-roughness conditions.

Keywords: moving roughness, non-Newtonian, transient, coupled method, differential deflection

NOTATION

b	Hertzian semidimension
E_1, E_2	Young's moduli of the two surfaces
E'	$2/E' = (1-\nu_1^2)/E_1 + (1-\nu_2^2)/E_2$
f_i	influence coefficients in the quadrature formula for $\mathrm{d}^2u/\mathrm{d}x^2$
g_i	influence coefficients in the quadrature formula for u
h	film thickness
h_s	constant in the film thickness formula
K	parameter for partitioning differential deflection pressure summation
ℓ	length of the finite element
n	number of mesh points
n_n	number of shape functions for the finite element
N_i	finite element shape functions
p	pressure
r	coordinate of the point relative to which elastic deflection is obtained
R	radius of relative curvature, $1/R = 1/R_1 + 1/R_2$
R_1, R_2	radius of curvature of the surfaces in line contact
R_a	surface roughness parameter
s	dummy integration variable in the elastic deflection formula
S	non-Newtonian parameter in the Reynolds equation
u	elastic deflection
U	mean entraining speed $= (U_1 + U_2)/2$
U_1, U_2	surface speeds relative to contact
w'	load per unit length
x	coordinate in the direction of rolling
x_c	position of the exit cavitation boundary
x_j	coordinate of the jth mesh point
x_1, x_n	first and last mesh points respectively
Z	constant in the viscosity expression determined from α
α	pressure coefficient of viscosity
γ, λ	constants in the compressibility equation
Δ	mesh spacing
η	viscosity
η_0	viscosity at zero pressure
ν_1, ν_2	Poisson's ratios of the two surfaces
ξ	slide–roll ratio $= 2(U_1 - U_2)/(U_1 + U_2)$
ρ	density
ρ_0	density at zero pressure
τ_0	representative or Eyring shear stress
ω	roughness geometry modification function

The MS was received on 21 December 2000 and was accepted after revision for publication on 1 March 2001.
**Corresponding author: Mechanical Engineering and Energy Studies Division, Cardiff School of Engineering, Cardiff University, Queen's Buildings, The Parade, PO Box 925, Cardiff CF24 0YF, Wales, UK.*

1 INTRODUCTION

Gears, rolling element bearings and rolling traction drives are crucial mechanical components in all kinds of

machinery used in vehicles, aerospace and process plant. (In these devices, forces are transmitted at heavily loaded (low-conformity lubricated contacts, giving rise to very high equivalent Hertzian elastic contact pressures (typically up to 1.5 GPa in gears and 4 GPa in bearings). As a result, fatigue, surface distress and wear of such contacts are the most common causes of failure. A high degree of protection from damage can be provided by an effective lubricant film which separates the surfaces in the region of their contact. The vital physical mechanism which can generate this separation is elastohydrodynamic lubrication (EHL). The main features of EHL for perfectly smooth surfaces (a dramatic increase in the viscosity of the lubricant at high pressures together with significant elastic flattening of the surfaces) are well understood from the early work of Grubin [**1**] and the pioneering numerical solutions of Dowson and Higginson [**2**]. However, an important feature of many engineering contacts, particularly those between the teeth of gears, is that the surfaces produced by present-day manufacturing methods leave roughness asperities that are significantly greater in scale than the predicted thickness of the EHL film based on classical smooth surface theory. Consequently they operate under conditions in which asperity–asperity interactions significantly affect both the deformation and the pressures within the nominal contact region; this regime of lubrication is described as 'micro-EHL'. In both spur and helical gears the teeth contact nominally along a line and the finishing process (typically grinding) leaves the lay of roughness perpendicular to the rolling/sliding direction of the teeth. Even the finest-quality gears manufactured in this way have typical peak-to-valley asperity dimensions which exceed the EHL film thickness calculated from smooth surface theory. Typical roughness average R_a values for a finely finished gear may well be 0.3 μm with peak-to-valley dimensions of about 2 μm as considered in the results section of this paper. Under heavily loaded high-temperature gear tooth conditions the classical Dowson–Higginson film thickness calculation may yield values of below 0.1 μm, and even thinner films are expected under roughness conditions. To gain a theoretical understanding of the processes at work in these real engineering contacts it is therefore necessary to direct modelling efforts at problems where the roughness features are at least an order of magnitude greater than the expected minimum films that can be generated by EHL action. Running in, which has been shown to smooth the surfaces to some degree, may mitigate the severity of potential individual asperity contacts but does not significantly change the relative magnitudes of roughness and the expected minimum film thickness.

In most engineering contacts there is a combination of rolling and relative sliding. In gears, for example, pure rolling only occurs instantaneously when the contact is at the pitch point of the gear pair. Sliding, with small clearances, necessitates a fluid rheology model that responds to the high shear rates that are present in the lubricant film. The EHL analysis of contacts must also take account of the time-dependent geometry as roughness features on both surfaces pass through the contact area. Conventional Newtonian piezoviscous lubricant models are known to overestimate significantly the surface shear stress, and therefore frictional traction, under sliding conditions. To remedy this deficiency a number of non-Newtonian lubricant models have been proposed by Bair and Winer [**3**] and Johnson and Tevaarverk [**4**] among others. The first of these models is based on experimental measurements of high-pressure shear behaviour in lubricant samples. The second approach, which is adopted in the current study, is based on analysis of disc machine experiments in the EHL regime and as such is particularly relevant to the problem under consideration.

The theoretical study of rough surface EHL has attracted many researchers over the last decade or so. Initial efforts involved stationary idealized roughness features [**5**–**7**], and real roughness features where the R_a value is significant compared with the film thickness were introduced by Kweh *et al*. [**8**]. Transient ('moving roughness') effects have been studied [**9**–**11**] using sinusoidal features or waveforms, and attention has been drawn to the important differences between Newtonian and non-Newtonian lubricant treatments in transient micro-EHL [**12**, **13**]. Real (or measured) roughness has been included in a transient line contact analysis [**14**, **15**] and, more recently, transient point contact analyses have been presented by Venner and Lubrecht [**16**] using sinusoidal features and Xu and Sadhegi [**17**] using measured roughness data. Where real roughness data have been incorporated in transient treatments, however, it is generally of a relatively low amplitude compared with the minimum film thickness in the numerical solution. This is indicative of the numerical difficulties that occur when the roughness features are large compared with the residual film thickness.

The contribution reported here significantly advances the study of micro-EHL by providing a new fast solution method, suitable for severe rough-surface thin-film conditions. The work stems from an investigation of the potential benefits (in terms of numerical stability and robustness) of full mathematical coupling of the elastic and hydrodynamic equations in the numerical solution scheme. This type of approach has been used by other workers in the past [**18**, **19**] but has not been generally adopted by the EHL community. The reason why fully coupled methods have not been more eagerly pursued seems to be the presumption that the elastic deflection integral, which causes the fully coupled solution scheme matrix to be fully populated, represents an intractable computing problem in spite of the method's potentially far greater robustness. In order to overcome this specific obstacle to further development of coupled methods in EHL, three of the present authors have developed a differential elastic deflection formulation [**20**, **21**]. The essential feature of the formulation is that it leads to a banded (as opposed to a fully populated) solution matrix (thus giving fast computing times) without compromising the major benefits of full coupling. With this

new approach, time-dependent analyses under very demanding rough-surface thin-film conditions can now be carried out. The formulation of the new coupled method is presented in detail in this paper together with initial results aimed at developing understanding of the pressure distributions and films generated between gear teeth under engineering conditions. At this stage the method has been developed for line contacts, but its extension to the geometry of point contacts is possible.

2 THEORETICAL BASIS

The equations to be solved are the non-Newtonian Reynolds equation for the fluid film after Conry *et al.* [**22**] incorporating the time-dependent squeeze-film term:

$$\frac{\partial(\rho h)}{\partial t} + U\frac{\partial(\rho h)}{\partial x} - \frac{\partial}{\partial x}\left(\frac{\rho h^3}{12\eta} S \frac{\partial p}{\partial x}\right) = 0 \tag{1}$$

The non-Newtonian factor S depends on the pressure, film thickness, sliding speed and pressure gradient according to

$$S = \frac{3(\Sigma\cosh\Sigma - \sinh\Sigma)}{\Sigma^3} \times \sqrt{1 + \frac{\eta^2(U_2 - U_1)^2}{\tau_0^2 h^2}\frac{\Sigma^2}{\sinh^2\Sigma}}$$

where

$$\Sigma = \frac{h}{2\tau_0}\frac{\mathrm{d}p}{\mathrm{d}x}$$

This formulation is based on the shear thinning rheological model proposed by Johnson and Tevaarwerk [**4**] found from experimental traction tests. An alternative limiting shear stress non-Newtonian model [**3**] may be considered but does not allow the factor S to be considered in closed form, a complication that is avoided in the present contribution but has been considered by authors and co-workers elsewhere [**23**].

The oil properties of density and viscosity are pressure dependent after Roelands [**24**] and Dowson and Higginson [**2**] respectively according to

$$\eta = \eta_0 \exp(\log\eta_0 + 9.67)[(1 + 5.1\times 10^{-9} p)^Z - 1] \tag{2}$$

and

$$\rho = \rho(p) = \rho_0\left(\frac{1 + \gamma p}{1 + \lambda p}\right) \tag{3}$$

The total elastic deflection of the surfaces treated as semi-infinite bodies is given by

$$u(x) = -\frac{4}{\pi E'}\int_{x_1}^{x_n} p(s)\ln\left|\frac{x - s}{r - s}\right| \mathrm{d}s \tag{4}$$

and together with the undeformed shape of the solid bodies gives the film thickness in the form

$$h(x,\ t) = u(x) + \frac{x^2}{2R} + \omega(x,\ t) + h_s \tag{5}$$

where $\omega(x, t)$ is the function giving the spatial and temporal distribution of deviations from the smooth surface shape given by the radius of relative curvature, R.

The present authors have shown elsewhere [**20**, **21**] that equation (4) may usefully be formulated in a differential form as

$$\frac{\mathrm{d}^2 u(x_j)}{\mathrm{d}x^2} = \sum_{\text{all } k} f_{k-j}\, p_k \tag{6}$$

The coefficients f_k decay rapidly as $|k|$ increases from zero in comparison with coefficients g_k obtained in evaluating equation (4) by the quadrature formula

$$u(x_j) = \sum_{\text{all } k} g_{k-j}\, p_k \tag{7}$$

This sharp decay ensures that the effect of pressure on the second derivative of deflection is highly localized. The pressure discretization used to obtain coefficients f in equation (6) is piecewise quadratic as presented in reference [**20**].

Equation (5) can be differentiated with respect to x twice and equation (6) used to give

$$\frac{\partial^2 h(x_j)}{\partial x^2} = \sum_{\text{all } k} f_{k-j}\, p_k + \frac{1}{R} + \frac{\partial^2\omega}{\partial x^2} \tag{8}$$

In the solution method described in this paper, equations (1) to (3) are used to describe the hydrodynamic action and equation (8) to model the elastic deflection process. Equation (8) requires two boundary values to be specified. The value of h at the entry boundary is an arbitrary constant used to obtain the required load, and equation (4) in the form of equation (7) is used to provide the second exit boundary condition required, as described in the Appendix.

3 NUMERICAL FORMULATION

In this work the spatial variation of the hydrodynamic equations is formulated numerically using the finite element method as described by Hughes *et al.* [**25**] for the second-order form of equation (1). The elastic deflection is incorporated using the differential deflection method. The accuracy of using the differential approach to the deflection integral in EHL analyses [**21**], and the compatibility of the

finite element formulation of the Reynolds equation with finite difference approaches to the problem over a wide range of operating conditions [**26**] has been established.

The basic formulation of equation (1) based on the Galerkin weighted residual approach yields

$$\int_{-\ell/2}^{\ell/2} N_i \frac{\partial(\rho h)}{\partial t}\,\mathrm{d}x + U\int_{-\ell/2}^{\ell/2} N_i \frac{\partial(\rho h)}{\partial x}\,\mathrm{d}x - \frac{1}{12}\int_{-\ell/2}^{\ell/2} N_i \frac{\partial}{\partial x}\left(\frac{\rho h^3}{\eta} S \frac{\partial p}{\partial x}\right)\mathrm{d}x = 0$$

where N_i are the shape functions adopted for the finite element treatment and ℓ is the length of the element. The integrations are over the length of the finite elements and limits of integration are omitted in subsequent equations for simplicity. Using the 'weak' formulation (ignoring the resultant boundary element term which cancels when the global matrix is assembled) and manipulating the second term gives

$$\int N_i \frac{\partial(\rho h)}{\partial t}\,\mathrm{d}x + U\int N_i\left(h\frac{\partial \rho}{\partial x} + \rho\frac{\partial h}{\partial x}\right)\mathrm{d}x + \frac{1}{12}\int \frac{\partial N_i}{\partial x}\frac{\rho h^3}{\eta} S \frac{\partial p}{\partial x}\,\mathrm{d}x = 0 \tag{9}$$

The time-dependent term is expressed using a centred difference and the spatial terms are expressed as a weighted sum of their values at two successive time steps to give

$$\begin{aligned} &-\int N_i \rho h\,\mathrm{d}x|^{t} + \int N_i \rho h\,\mathrm{d}x|^{t+\Delta t} \\ &+ \theta\Delta t\left[U\int N_i\left(h\frac{\partial \rho}{\partial x} + \rho\frac{\partial h}{\partial x}\right)\mathrm{d}x + \frac{1}{12}\int \frac{\partial N_i}{\partial x}\frac{\rho h^3}{\eta} S\frac{\partial p}{\partial x}\,\mathrm{d}x\right]^{t} \\ &+ (1-\theta)\Delta t\left[U\int N_i\left(h\frac{\partial \rho}{\partial x} + \rho\frac{\partial h}{\partial x}\right)\mathrm{d}x + \frac{1}{12}\int \frac{\partial N_i}{\partial x}\frac{\rho h^3}{\eta} S\frac{\partial p}{\partial x}\,\mathrm{d}x\right]^{t+\Delta t} = 0 \end{aligned} \tag{10}$$

The superscripts in equation (10) indicate the time at which each of these terms is evaluated. The equation is implicit for values of $\theta < 1.0$ and becomes the standard Crank–Nicolson method when the weighting is the usual value of $\theta = 0.5$. In Crank–Nicolson form the time derivative, which is evaluated at the mesh point mid-way between time steps, has second-order accuracy in $\Delta t/2$.

Using standard interpolation formulae and collecting terms at the same time step together, equation (10) becomes

$$\begin{aligned} &\int N_i \tilde{\rho}(N_j h_j)\,\mathrm{d}x|^{t+\Delta t} + (1-\theta)\Delta t \\ &\times\left\{U\int N_i\left[\frac{\partial \tilde{\rho}}{\partial x}(N_j h_j) + \tilde{\rho}\left(\frac{\partial N_j}{\partial x}h_j\right)\right]\mathrm{d}x\right\}^{t+\Delta t} \\ &\times(1-\theta)\Delta t\left[\frac{1}{12}\int \frac{\partial N_i}{\partial x}\frac{\tilde{\rho}\tilde{h}^3}{\tilde{\eta}}\tilde{S}\left(\frac{\partial N_j}{\partial x}p_j\right)\mathrm{d}x\right]^{t+\Delta t} \\ &= \int N_i \tilde{\rho}\tilde{h}\,\mathrm{d}x|^{t} - \theta\Delta t\left[U\int N_i\left(\tilde{h}\frac{\partial \tilde{\rho}}{\partial x} + \tilde{\rho}\frac{\partial \tilde{h}}{\partial x}\right)\mathrm{d}x + \frac{1}{12}\int \frac{\partial N_i}{\partial x}\frac{\tilde{\rho}\tilde{h}^3}{\tilde{\eta}}\tilde{S}\frac{\partial \tilde{\rho}}{\partial x}\,\mathrm{d}x\right]^{t} \end{aligned} \tag{11}$$

where the repeated subscript j indicates summation and averaged quantities are as defined in the Appendix.

The elastic deflection is given by equation (8) which is expressed numerically using finite differences as

$$h_j - \frac{h_{j+1}}{2} - \frac{h_{j+1}}{2} + \frac{\Delta^2}{2}\sum_{|k-j|\leqslant K} f_{k-j}p_k = -\frac{\Delta^2}{2}\sum_{|k-j|>K} f_{k-j}p_k - \frac{\Delta^2}{2R} + \varphi_j - \frac{\varphi_{j+1}}{2} - \frac{\varphi_{j+1}}{2} \tag{12}$$

The pressure summation is partitioned into contributions within K mesh spaces of the point of application of the equation which appear on the left-hand side of equation (12), and the remainder that appear on the right-hand side. These right-hand side contributions are linearized during the numerical solution and are evaluated using pressures from the time step's previous iterative cycle.

Equations (11) and (12) are solved as a pair of coupled equations and are arranged in matrix form as follows:

$$\begin{bmatrix} \mathbf{R}_p & \mathbf{R}_h \\ \mathbf{E}_p & \mathbf{E}_h \end{bmatrix}_{i,j}\begin{Bmatrix} p_j \\ h_j \end{Bmatrix} = \begin{Bmatrix} \mathbf{R}_r \\ \mathbf{E}_r \end{Bmatrix}_i \tag{13}$$

where $\mathbf{R}_p$, $\mathbf{R}_h$ and $\mathbf{R}_r$ are the coefficient submatrices corresponding to the Reynolds equation and $\mathbf{E}_p$, $\mathbf{E}_h$ and $\mathbf{E}_r$ are those corresponding to the differential deflection equation. The entries in these submatrices are given in the Appendix.

A time step thus consists of evaluating $\mathbf{R}_r$ from the pressure and film thickness distribution for the previous time step. These pressure and film thickness distributions are taken as a first approximation for the solution for the new time step and used to evaluate coefficients $\mathbf{R}_p$ and $\mathbf{R}_h$,

and also the pressure-dependent contribution to $\mathbf{E}_r$. The remaining coefficients in equation (13) are fixed for the time step.

Equation (13) is then solved to give the next approximation to the distributions of pressure and film thickness at the new time step. The coefficients $\mathbf{R}_p$, $\mathbf{R}_h$ and $\mathbf{E}_r$ are then recalculated based on the new approximation for $p(x, t+\Delta t)$ and $h(x, t+\Delta t)$ and the process is repeated until converged values for $p(x, t+\Delta t)$ and $h(x, t+\Delta t)$ are obtained. The time step adopted is typically $\Delta/(4U_{\max})$ where $U_{\max}$ is the larger of the two surface velocities. When real rough surface profiles are used to define the surface texture, as opposed to smooth analytic functions, interpolation must be used to determine the surface geometry at each time step from the measured roughness profiles. The geometry changes imposed on a model between time steps are greatest for the faster-moving surface and the time step used is based on this maximum surface velocity in order to regularize the interpolation of the surface geometry. In numerical experiments carried out with different time step values, $\Delta/(4U_{\max})$ has been found to give results that are independent of the value selected. For this value of the time step the calculation of $p(x, t+\Delta t)$ and $h(x, t+\Delta t)$ typically takes five to ten iterations. The value of K adopted is 7, giving a bandwidth for the coupled problem of 30. The time taken to solve equation (13) is $O(nK^2)$ [**20**] so that, for large numbers of mesh points, evaluation of $\mathbf{E}_r$ is the dominant computation task.

The time-dependent solution is started by solving the smooth surface problem. This is achieved within the same software scheme by setting $\mathbf{R}_r$ to zero and using a very long time step which effectively negates the last term in $\mathbf{R}_h$. The Hertz pressure is used for the initial pressure distribution. Once this solution has been obtained, the surfaces move forwards for the next time step and the surface modification function $\varphi(x, t)$ is introduced. This function has a value of zero over the whole of the solution space initially, and the surface modification features then enter the solution space progressively at the inlet boundary. In this way the time-dependent solution obtained corresponds to the physical problem of smooth rollers whose surfaces have roughness upstream of the contact that gradually moves into the contact region. Consequently a large number of time steps are used to ensure that the roughness detail has progressed to encompass the whole of the contact.

For cases where the surface deviations are given by profilometer trace information as presented in Section 5 the surface modification function $\varphi(x, t)$ is not known analytically. This requires interpolation between data points in the trace(s) in order to determine the values of $\varphi(x_i, t)$ at all time steps. It is also necessary to interpolate between profile data points if the computing mesh is finer than the resolution at which the profilometer trace was acquired. (This will often be the case as the profilometer diamond stylus tip shape is such that profile resolution finer than 2 μm is not meaningful.) A cubic spline interpolation is used to provide surface heights at intermediate points between the data points as required, both for using computing meshes that differ from the profile trace spacing and during the time-dependent solution. In this way the surface is always represented by the same collection of piecewise cubic splines. Slope continuity is an important consideration in considering squeeze-film effects in time-dependent problems and with a cubic spline interpolation procedure both the profile height and its slope are continuous. The computing nodes are fixed relative to the point of contact so that there is no time dependence of the basic curvature terms of the two surfaces.

4 EXIT CAVITATION

At the exit to an EHL contact the pressure falls to zero at an unknown position where the Reynolds boundary condition

$$p = \frac{\partial p}{\partial x} = 0$$

is usually taken to apply. In numerical solutions this is commonly interpreted as a condition that prevents the lubricant pressure from falling below zero.

Such a condition is relatively easy to apply in an iterative solution where the pressure is the only active variable, but in the coupled approach described in this paper some care is necessary. Setting negative pressures to zero within the back substitution as equation (13) is solved does not remove the influence of those negative values on the remaining pressures and film thickness values. The method used is as follows.

In the steady state initial solution the position of the exit cavitation boundary, x_c, is a variable that is initially set to x_n. This is the position of the node at which the exit boundary condition $p = 0$ is applied. As the solution proceeds, negative pressures that occur upstream of x_c are set to zero and the cavitation position is moved upstream progressively until negative pressures are no longer calculated. For hydrodynamic rows of equation (13) downstream of x_c the Reynolds equation is replaced by the condition $p = 0$. Thus, for all values of i such that $x_i > x_c$,

$$\mathbf{R}_p = 1 \text{ for } j = i, \qquad \mathbf{R}_p = 0 \text{ for } j \neq i$$

$$\mathbf{R}_h = 0 \text{ for all } j, \qquad \mathbf{R}_r = 0$$

The flow at the cavitation node, i.e. at x_c, is calculated from its value at the Gauss points in the cavitating element. This flow is partitioned between each of the moving solid surfaces downstream of x_c. If during the calculation the flow at the first cavitated point, $x > x_c$, is found to exceed ρUh, then the film is re-established at that node and the cavitation boundary moves downstream. In this way the

steady state exit boundary position is located to the nearest mesh point.

Having located the exit cavitation position for the steady state, it is necessary to allow it to migrate upstream and downstream within the time-dependent solution as called for by the passage of individual roughness features through the exit. This requires account to be taken of the flow within each cavitated element in the time-dependent formulation of the Reynolds equation, and the cavitated fluid is taken to move with the speed of the surface to which it is attached. To check this procedure the load fixing parameter h_1 has been varied steadily over 100 time steps to a new fixed value until flow disturbances caused by this squeezing of the film have propagated out of the contact. The time-dependent solution then becomes the steady state solution for the new value of h_1. Comparing the exit boundary position established with a standard steady state solution at the same h_1 value shows agreement of x_c to within one mesh spacing.

Cavitation at micro-asperity contacts within the contact region with downstream re-formation of the film can be treated using this general approach in principle. This phenomenon has been reported in stationary roughness examples [**27**] but does not occur in the transient cases discussed in the current paper. Recent work by the present authors suggests that it can be provoked in more extreme circumstances, but the importance of reservoirs of oil in pressurized valley features downstream of transient microcontacts in maintaining a full film cannot be overstated.

5 RESULTS

Results are presented for the time-dependent cases of a single rough surface running against a smooth surface, and for two rough surfaces running against each other.

5.1 Single rough surface

The rough surfaces used are those from profilometer traces taken from axially finished steel discs used in scuffing experiments [**28**]. The profiles concerned were taken from the unscuffed part of a test disc that had experienced running at a heavy load. The asperity height distribution is therefore negatively skewed by the running-in process from its initial almost Gaussian form. The discs were axially finished using aerospace manufacturing procedures in order to replicate as closely as possible the surface finish found in gear teeth in aerospace auxiliary gearbox applications which were the focus of the experimental work. Theoretical results have been obtained for a sequence of 11 slide–roll ratios of $\xi = \pm 2, \pm 1.2, \pm 0.6, \pm 0.3, \pm 0.15$ and 0.0 (pure rolling). For cases having one smooth and one rough surface the convention adopted is that positive values of ξ have the rough surface moving faster and the case $\xi = -2$ has a stationary rough surface for which the problem is quasi-steady. A series of three entraining velocities was used to simulate different film thickness conditions. These velocities and the oil specification cover the experimental conditions used [**28**]. The results described in this paper for a single rough surface are taken from the two lower-velocity cases. Results for a preliminary analysis of the 25 m/s case have been presented by the present authors elsewhere [**29**]. Table 1 specifies the parameters for the analysis.

Visualization of solutions to moving roughness (time-dependent) problems is best achieved by constructing an animated sequence of film and pressure distributions for successive time steps. In viewing such an animation for the cases modelled in this paper it is seen that the film thickness on an individual microcontact is formed by the rolling/squeezing motion of the surfaces at the inlet to the corresponding Hertzian area. The deformed shape of the asperity stabilizes in the first quarter of the dry contact area and then progresses through the contact in a broadly unaltered way. The pressure distribution associated with the deformed shape is a substantial perturbation to the smooth surface pressure distribution and keeps pace with the microcontact as it moves through the Hertzian area. Travelling waves at the average surface velocity that have been reported in studies of sinusoidal roughness with Newtonian lubricants are not seen in the current work as a result of the much reduced effective viscosity of the more realistic non-Newtonian fluid model adopted.

The conditions assumed have a corresponding Hertzian contact dimension $b = 0.36$ mm and for smooth surface conditions the maximum pressure is 1.07 GPa. The finite element mesh for the solutions presented has 192 nodes in the Hertzian dimension and, as the inlet boundary is located at $-3b$, some 3000 time steps are needed for the roughness profile to cover the entire contact. Figure 1 shows the pressure and film thickness at time step 5500 for the case having $\xi = -0.6$ and $U = 10$ m/s. This entrainment velocity results in minimum film thicknesses of the order of 0.04 μm as the different surface roughness features pass through the contact area which is only 6 per cent of the corresponding Dowson–Higginson smooth surface value. The figure also shows the undeformed surface roughness profile to which a negative offset has been added for

Table 1 Conditions assumed for the real roughness analyses

R_1 and R_2	19.05 mm
τ_0	5.0 MPa
w'	600 kN/m
η_0	0.0048 Pa s
U	5, 10 and 25 m/s
E_1 and E_2	206.8 GPa
ν_1 and ν_2	0.3
α	11.1 GPa^{-1}

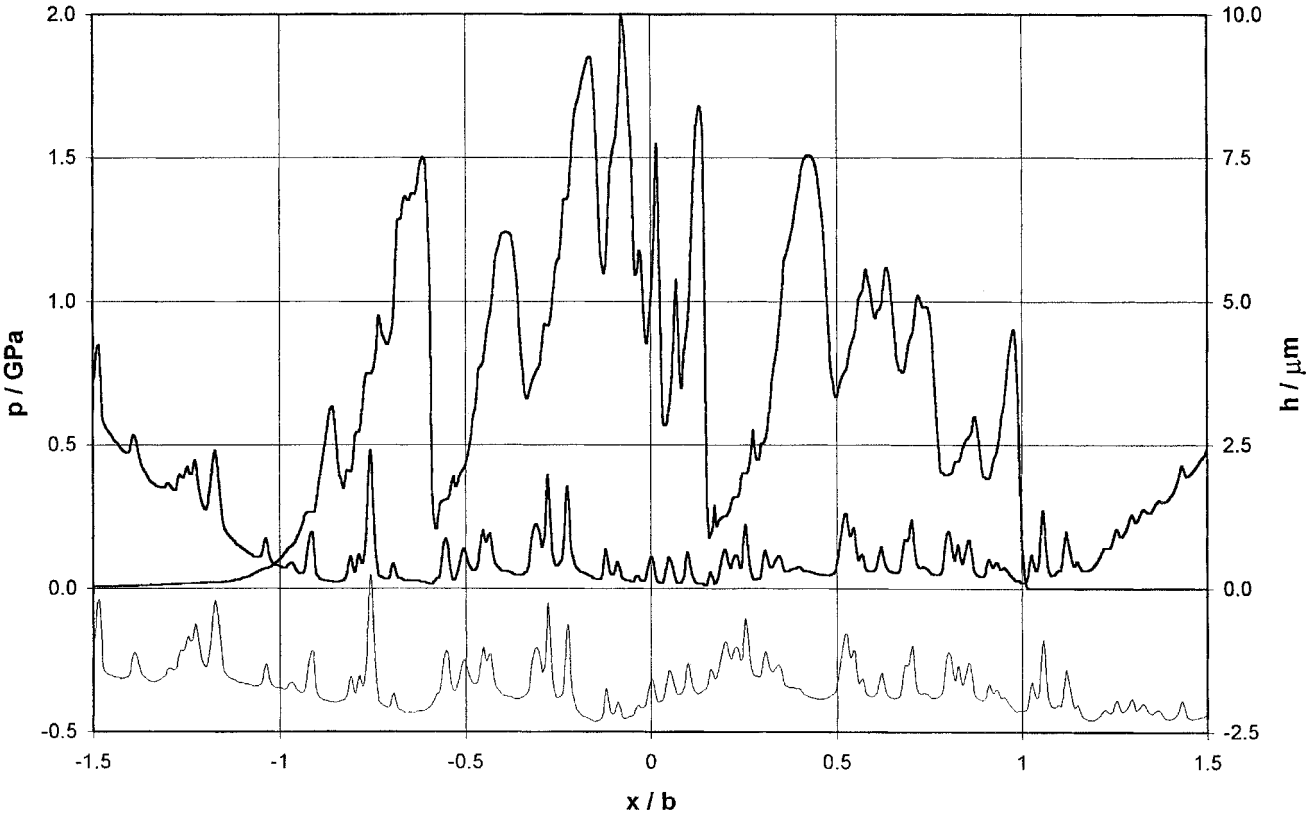

Fig. 1 Pressure (upper curve) and film thickness distributions at time step 5500 for $\xi = -0.6$ and $U = 10$ m/s. Also shown (light curve) is the undeformed roughness profile at this time step with a negative offset for clarity. Note that the solid surface is above the profile

clarity. This clearly demonstrates the alignment of undeformed and deformed features within the EHL film. The shapes adopted by micro-asperities are formed in the inlet and remain effectively unchanged as they traverse the contact. This is illustrated by consideration of Figs 2 and 3 which show the situation at time steps 6000 and 6500 respectively. The 500 time step interval between these figures corresponds to a distance moved by the rough surface of $0.65b$ and it can be seen that during each of these intervals the microcontacts within the contact have progressed by this distance and their deflected shape remains similar. For example, the microcontact in the range $-0.8 < x/b < -0.6$ in Fig. 1 is centred at $x/b = 0$ in Fig. 2 and at $x/b = 0.65$ in Fig. 3, and the similarity between the pressure distributions at these locations is clear. The film thickness over a short length of 100 mesh points (including the feature referred to above) is examined at five positions during its traverse of the contact area in Fig. 4. These positions are each separated by 500 time steps. Figure 4a shows the profile section in the inlet as it enters the contact area in three positions within the contact area and as it leaves the contact area. The undeformed profile is also included and the figure shows that the film shape corresponding to a microcontact feature remains almost the same as it traverses the contact. The small differences can be seen in Fig. 4b which shows the profile section at the three central positions in greater detail. The microcontacts can be seen to form film thickness features that are convergent from left to right. Figure 5 shows the deviations of pressure in these three cases from the smooth surface pressure distribution at the corresponding position in the contact. These pressure perturbations demonstrate that the deflection required of the asperity by the EHL model is substantially the same at the three positions.

Figure 6 shows the result for time step 6000 when the direction of sliding is reversed so that $\xi = 0.6$. Comparison with Fig. 2 shows that the deformed shapes of the microcontacts are now different with the gentler pressure gradients to the right of contact features and the steepest pressure gradients to the left. Figures 7a and b show the same profile section as examined in Fig. 4 during its traverse of the contact area for this case ($\xi = 0.6$) where relative sliding is in the opposite direction. Again the film thickness is seen to be very similar during the traverse of the contact but now the microcontacts deform so as to be convergent from right to left. It can be seen in each case that the microcontacts take on deformed shapes that cause the oil film to be convergent in the direction of entrainment *relative to the asperity*. In Fig. 4 the rough surface is moving the slowest so that, relative to the asperity, the entrainment is from left to right, but in Fig. 7 the rough surface is moving faster so that entrainment is from right to left relative to the asperity. The velocity relative to the asperity thus takes on the role of (twice) the entrainment

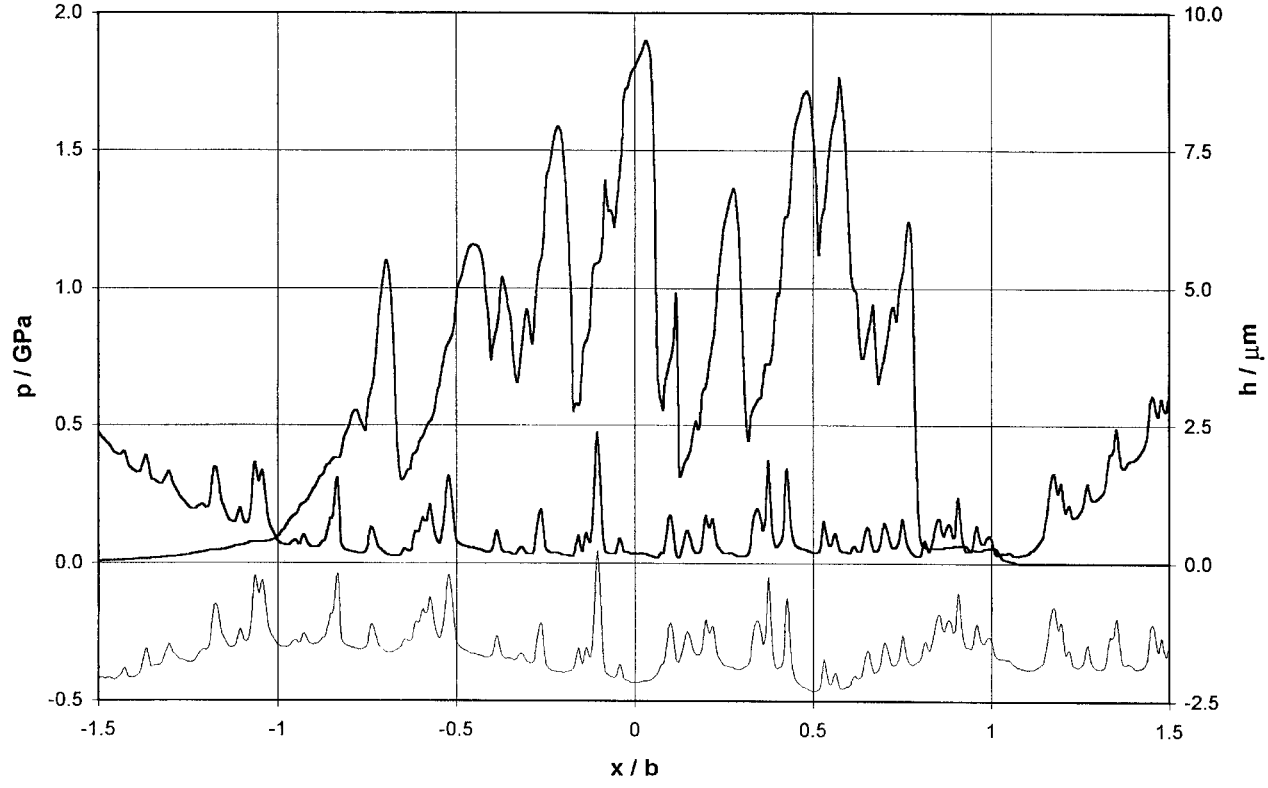

Fig. 2 Pressure (upper curve) and film thickness distributions at time step 6000 for $\bar{\xi} = -0.6$ and $U = 10$ m/s. Also shown (light curve) is the undeformed roughness profile at this time step with a negative offset for clarity. Note that the solid surface is above the profile

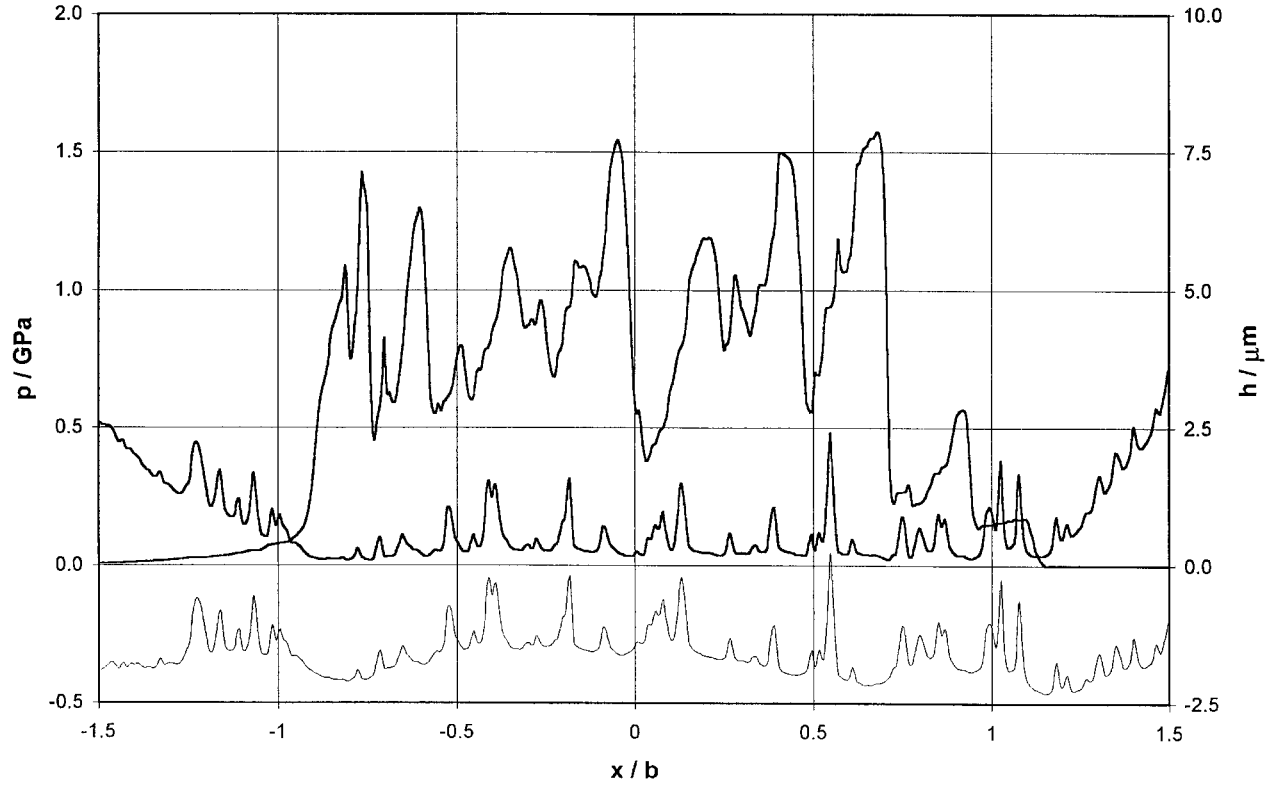

Fig. 3 Pressure (upper curve) and film thickness distributions at time step 6500 for $\bar{\xi} = -0.6$ and $U = 10$ m/s. Also shown (light curve) is the undeformed roughness profile at this time step with a negative offset for clarity. Note that the solid surface is above the profile

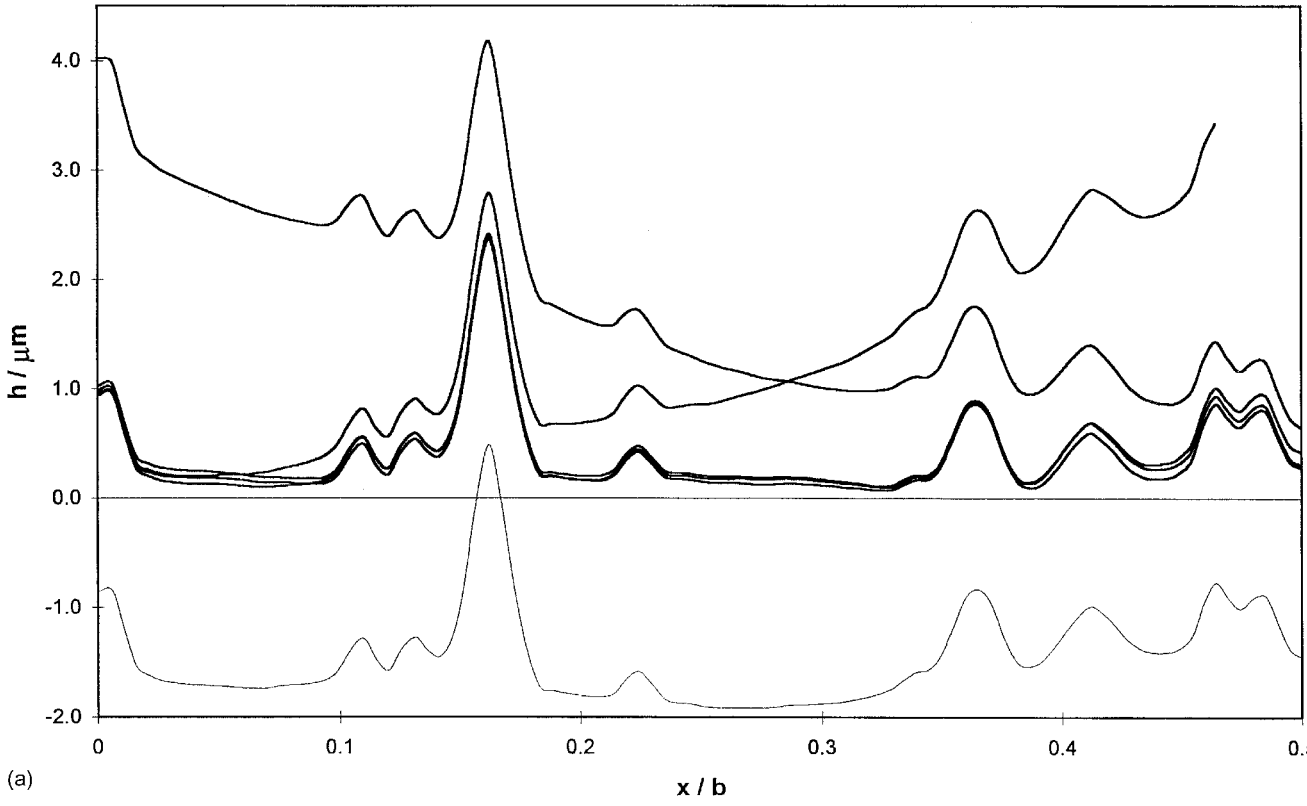

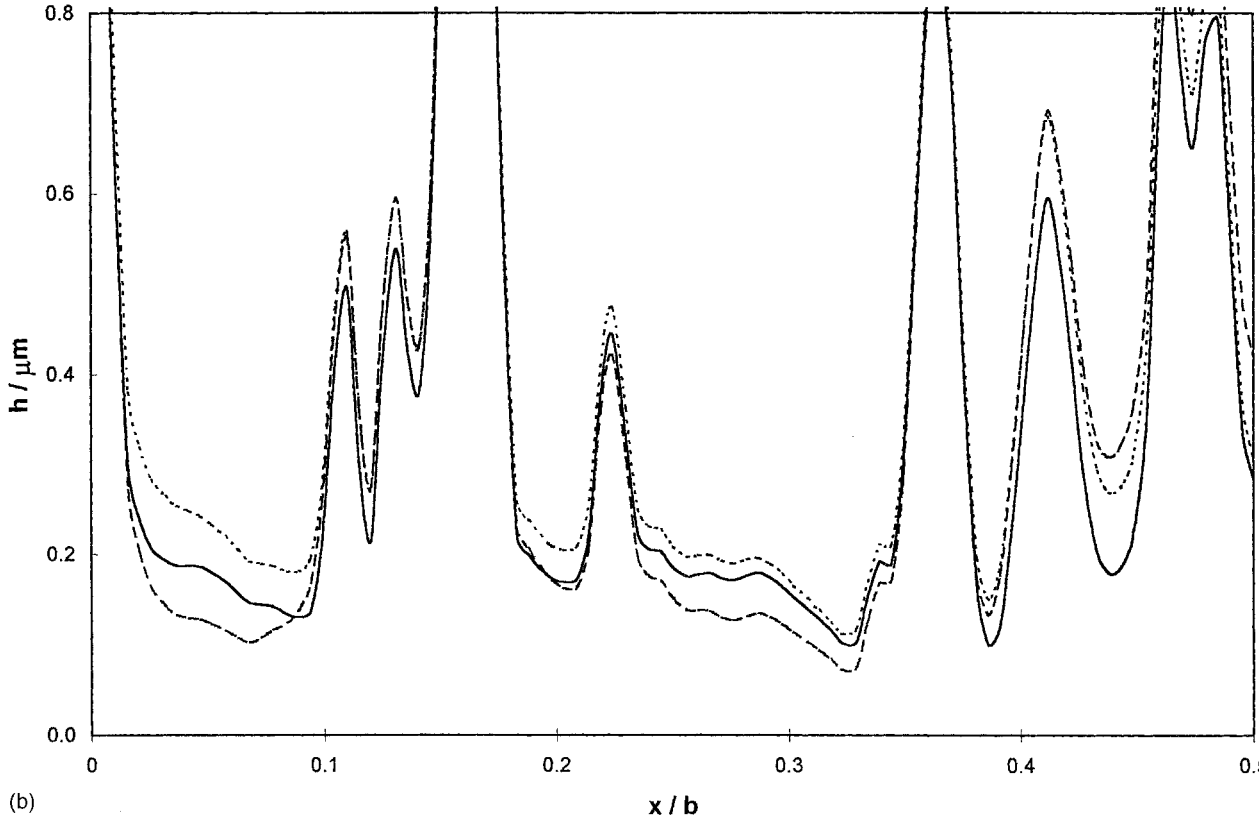

Fig. 4 Film thickness for a particular 180 μm length of roughness profile at five positions during traverse of contact for case $\xi = -0.6$ and $U = 10$ m/s. (a) Five film thickness traces together with offset undeformed profile (solid surface above profile). (b) Detailed view of traces centred at $x/b = -0.65$ (– – –), $x/b = 0$ (——) and $x/b = +0.65$ (· · · · · ·)

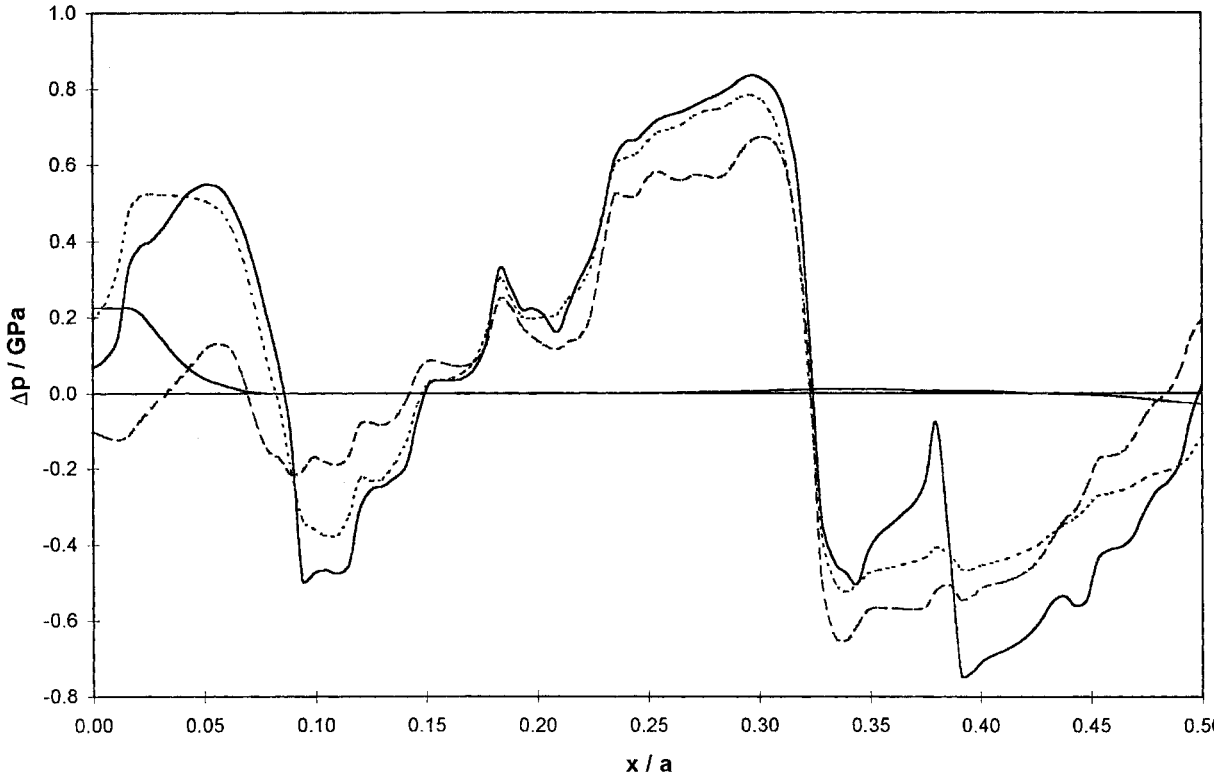

Fig. 5 Deviation of pressure from smooth surface distribution for the cases shown in Fig. 4b. Traces centred at $x/b = -0.65$ (– – –), $x/b = 0$ (——) and $x/b = +0.65$ (· · · · · ·)

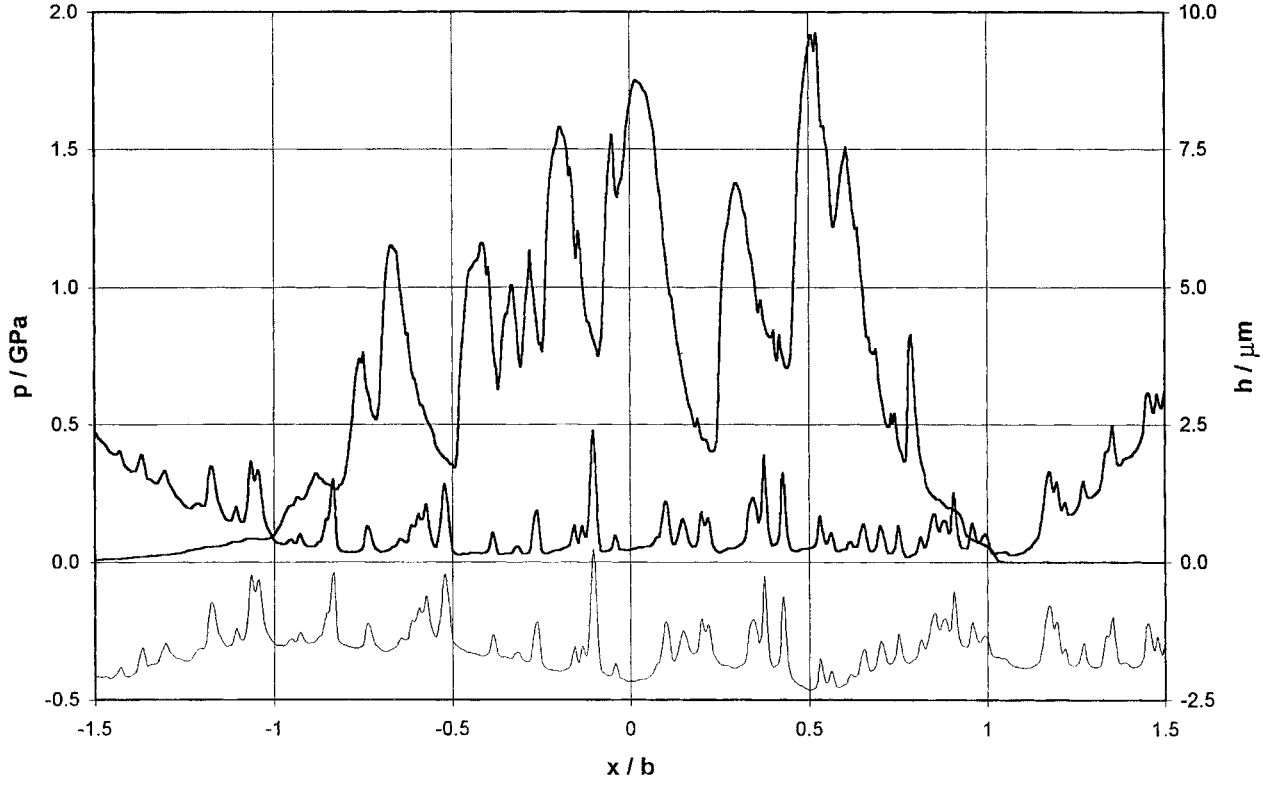

Fig. 6 Pressure (upper curve) and film thickness distributions at time step 6000 for $\bar{\xi} = +0.6$ and $U = 10$ m/s. Also shown (light curve) is the undeformed roughness profile at this time step with a negative offset for clarity. Note that the solid surface is above the profile

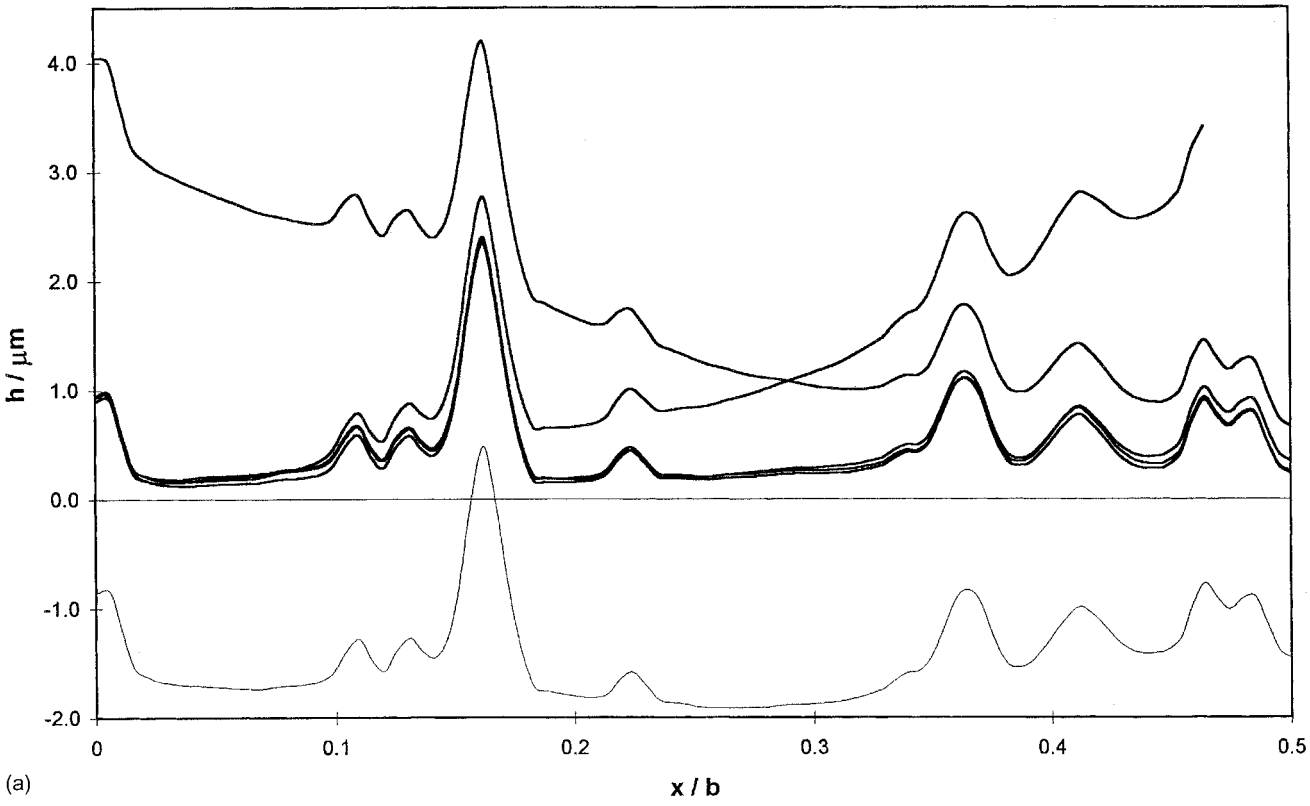

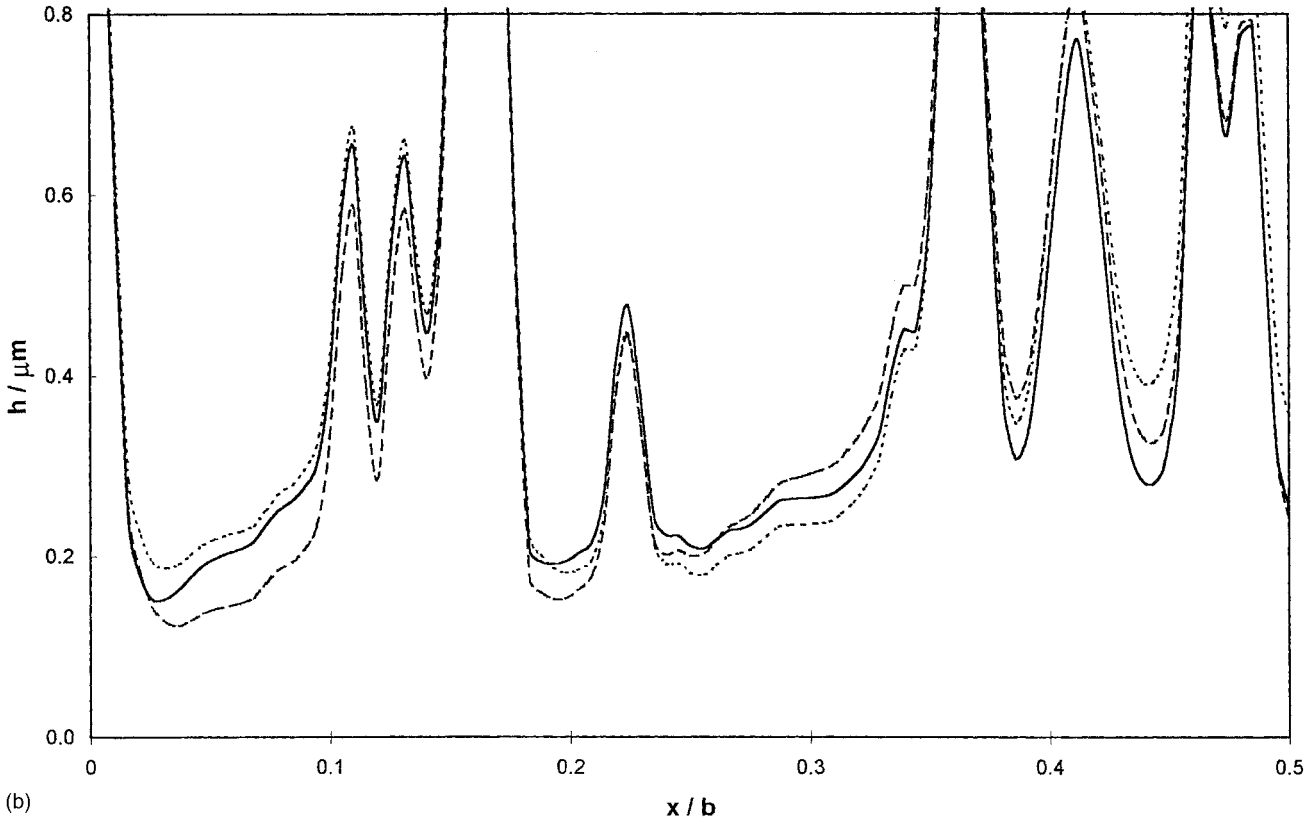

Fig. 7 Film thickness for a particular 180 μm length of roughness profile at five positions during traverse of contact for $\bar{\xi} = +0.6$ and $U = 10$ m/s. (a) Five film thickness traces together with offset undeformed profile (solid surface above profile). (b) Detailed view of traces centred at $x/b = -0.65$ (– – –), $x/b = 0$ (——) and $x/b = +0.65$ (· · · · · ·)

velocity once the microcontact has moved into the Hertzian contact area. Sliding is therefore seen to have a hydrodynamic effect in micro-EHL which is absent in smooth–smooth contacts in which film formation is determined purely by the rolling velocity.

It is interesting that waves travelling at the contact's entrainment velocity that have been reported by other investigators are not seen in these results. This would seem to be due to the inclusion in this work of the non-Newtonian lubricant formulation that allows pressure gradients to cause fluid flow in the high pressure region. The deep valley features that characterize real, run-in surfaces may also be a significant factor in eliminating the travelling waves seen in other numerical models as they contain significant reservoirs of lubricant in comparison with the flow perturbations induced by surface features at the inlet. This 'storage' capability may influence this aspect of the results by absorbing any travelling flow pertubations by compression.

The importance of entrainment relative to the asperity is emphasized by the results shown in Fig. 8. This shows the film thickness of the profile section at the same contact position for the full range of slide–roll ratios. The film thickness distribution for each case is offset compared with the others to enable comparison. It is clear that the cases having negative slide–roll ratios form a family of EHL responses to the rough surface with the asperity being deformed to generate a film convergent from left to right. The cases having positive slide–roll ratios form another family of responses with the film convergent from right to left. The case of pure rolling that is also included is different as it does not generate entrainment relative to the asperity within the contact area. For this case the pressure response is markedly different, as can be seen in Fig. 9. The asperity shape persists as formed in the inlet region, and the pressure is much more sensitive to the details of surface roughness, responding to each deviation in height, even within the deep valleys.

Figure 10 shows time step 6000 for conditions $\xi = -0.6$ and $U = 5$ m/s. The film thicknesses are now smaller than those in the corresponding 10 m/s case shown in Fig. 2, with minimum values of the order of 0.02 μm as the different surface roughness features pass through the contact area. The corresponding Dowson–Higginson smooth surface value for this condition is 0.14 μm. The increased conformity of the microcontacts required by this thinner film regime causes an increased response of pressure to the finer scale of roughness features, but the predominant effect remains that of a series of microcontacts that progress almost unaltered through the contact. Figure 11 shows the film thicknesses of the profile section considered previously for each slide–roll ratio at this lower

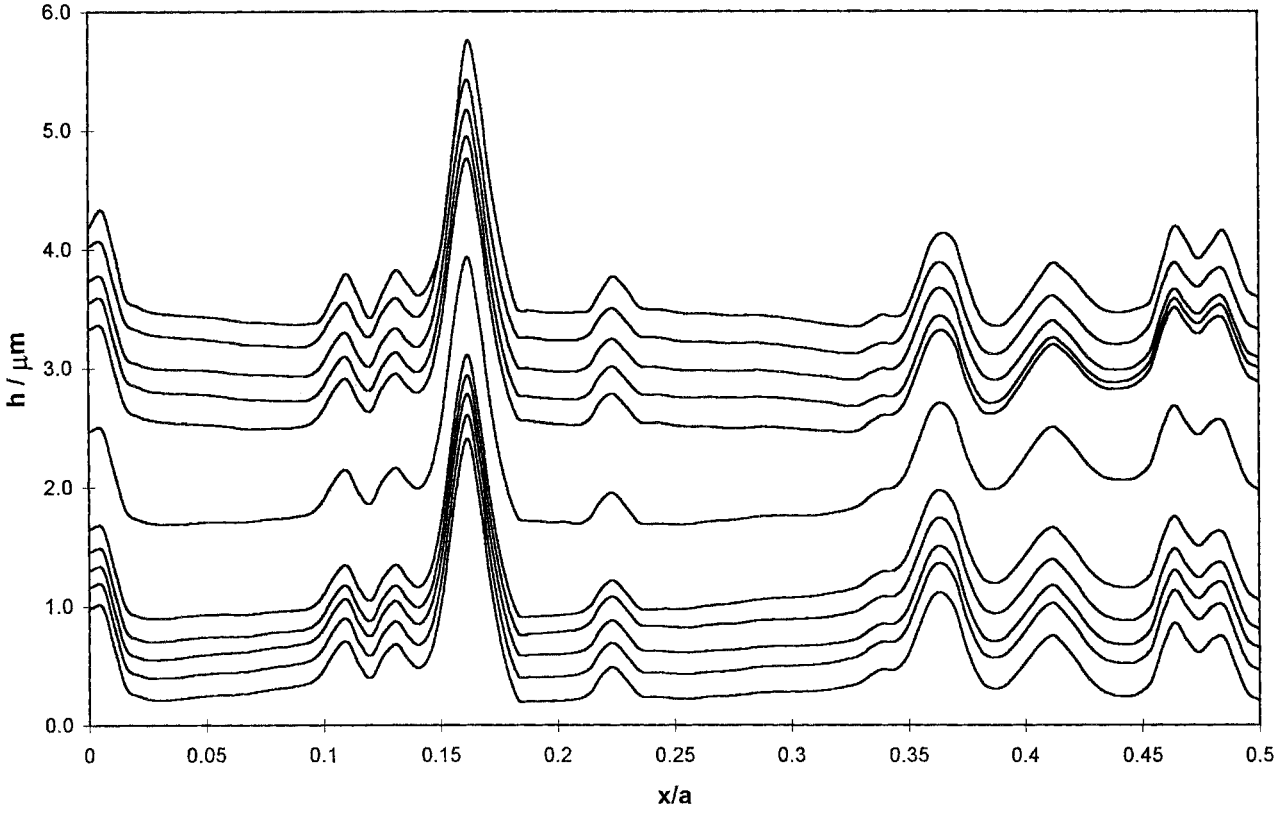

Fig. 8 Film thickness for the particular 180 μm length of roughness profile at the centre of the contact for $U = 10$ m/s and $\xi = -2$ (highest curve), −1.2, −0.6, −0.3, −0.15, 0, 0.15, 0.3, 0.6, 1.2 and 2.0 (lowest curve). Each film thickness curve is offset from its neighbours by 0.2 μm; the curve for $\xi = 0$ is offset by 0.6 μm

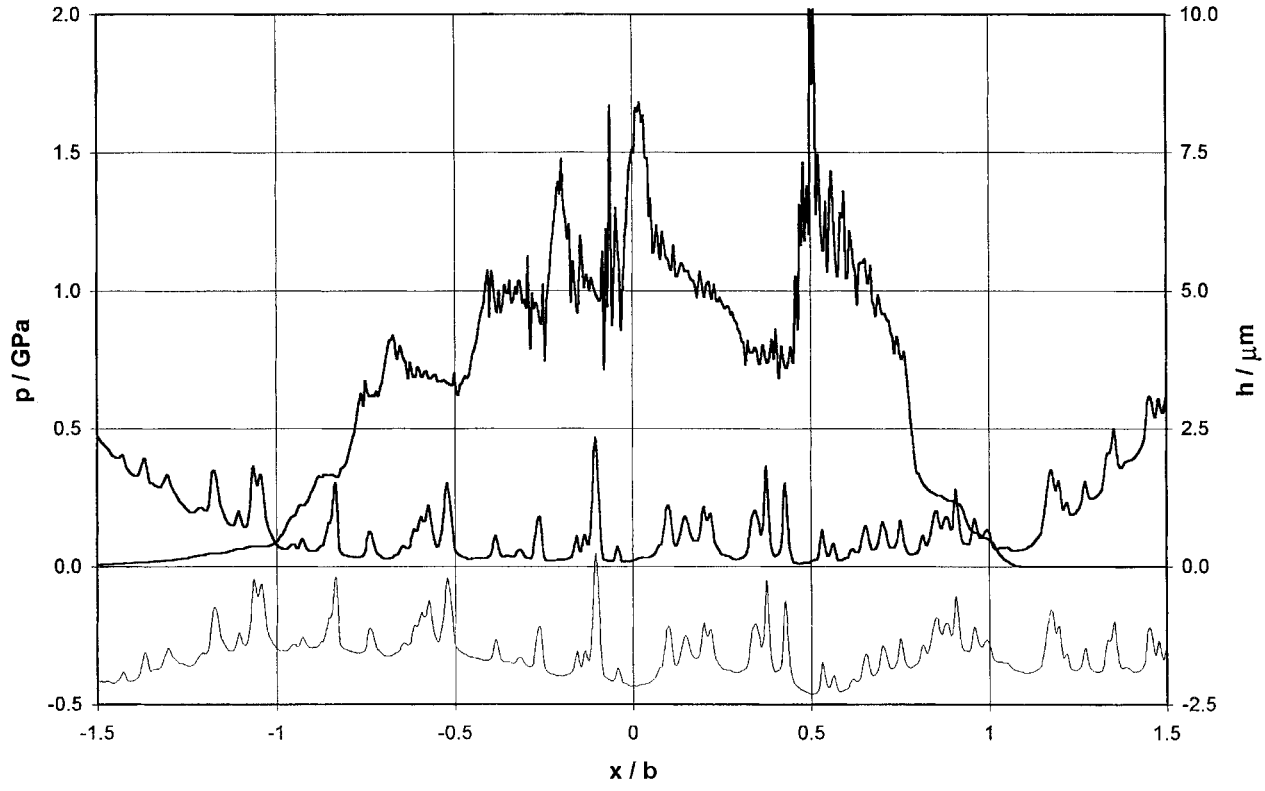

Fig. 9 Pressure (upper curve) and film thickness distributions at time step 6000 for the pure rolling case with $U = 10$ m/s. Also shown (light curve) is the undeformed roughness profile at this time step with a negative offset for clarity. Note that the solid surface is above the profile

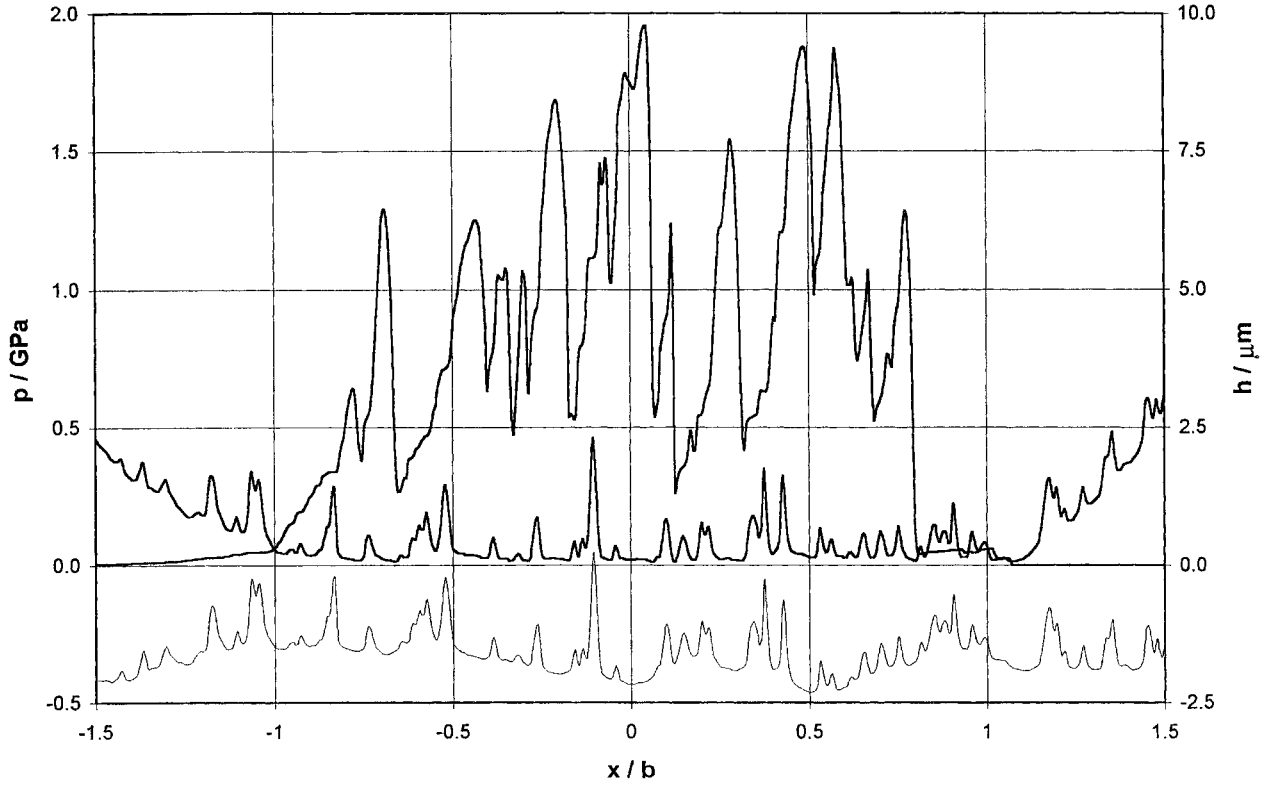

Fig. 10 Pressure (upper curve) and film thickness distributions at time step 6000 for $\bar{\xi} = -0.6$ and $U = 5$ m/s. Also shown (light curve) is the undeformed roughness profile at this time step with a negative offset for clarity. Note that the solid surface is above the profile

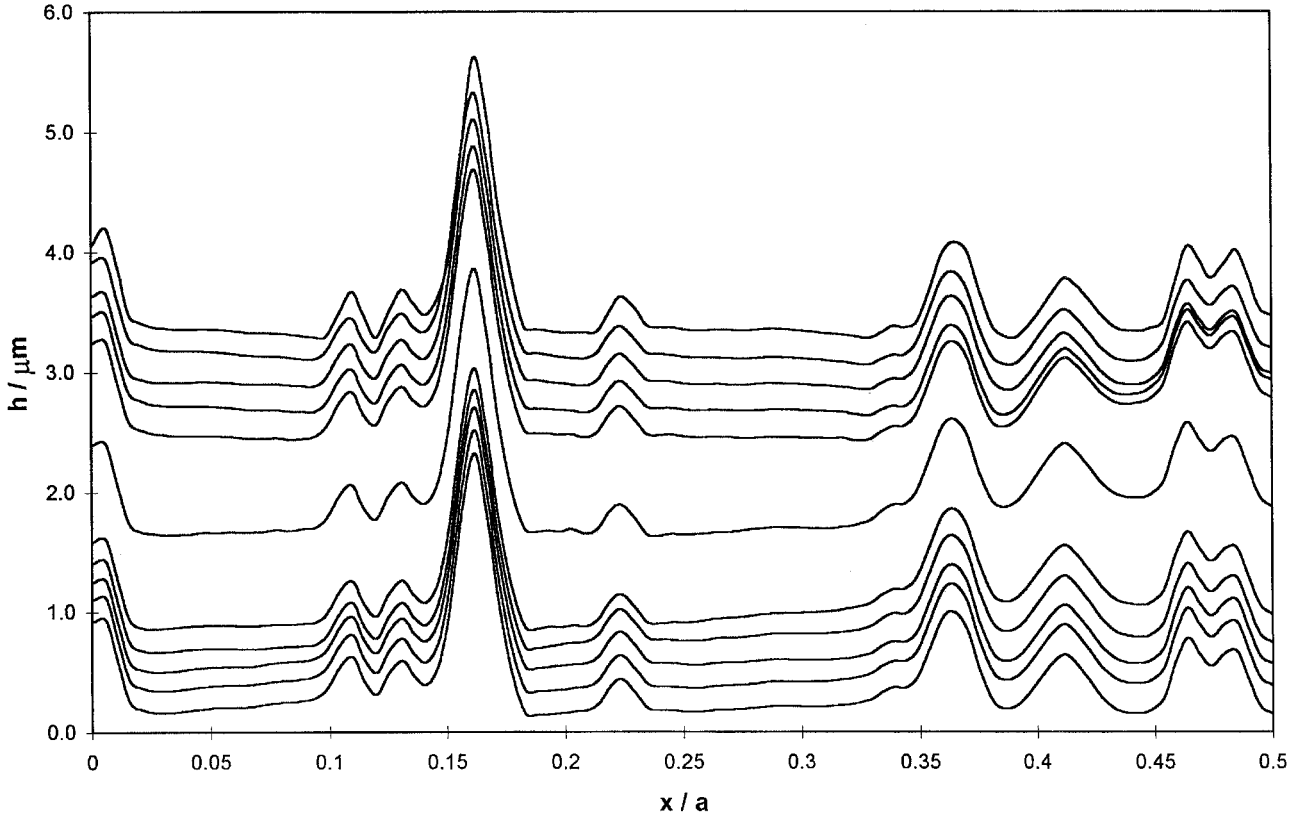

Fig. 11 Film thickness for the particular 180 μm length of roughness profile at the centre of the contact for $U = 5$ m/s and $\xi = -2$ (highest curve), -1.2, -0.6, -0.3, -0.15, 0, 0.15, 0.3, 0.6, 1.2 and 2.0 (lowest curve). Each film thickness curve is offset from its neighbours by 0.2 μm; the curve for $\xi = 0$ is offset by 0.6 μm

entrainment velocity and again shows two distinct families of EHL responses corresponding to positive and negative slide–roll ratios.

5.2 Two rough surfaces

Animated sequences are particularly useful in visualizing the effect of incorporating surface roughness on both surfaces. Single-time-step snapshots are shown in Figs 12 to 14 for a case with $\xi = -0.3$ and $U = 25$ m/s. Again it can be seen that the pressure distribution shows deviations from the Hertzian shape that are on the scale of the larger microcontacts rather than the individual roughness features. Indeed in the figures shown the elastohydrodynamic lubricant clearly causes load sharing between the macro-contacts with relatively little influence of the finer scale of roughness on the pressure distribution. The situation is complicated by the interaction of such features on the two surfaces. Some prominent features tend to maintain an associated pressure deviation as they move in and out of intimate contact with different features on the other surface for example the feature of the lower surface just to the right of the origin in Fig. 12 has a similar pressure deviation in Fig. 13 where it is located at $x = 0.5b$. On the other hand the lower surface flat topped feature at $x \approx -0.6b$ in Fig. 12 is associated with a relatively high pressure whereas in Fig. 13 where it has progressed to a position $x \approx -0.1b$ its pressure is relatively low as is the case in Fig. 14 at position $x = 0.4b$. In general the inclusion of roughness on both surfaces leads to a reduction in the minimum film thickness in comparison with the case with one smooth surface. The results shown are for the higher entrainment velocity of 25 m/s which enables a full film to be maintained throughout the analysis. At lower entrainment speeds the combined roughness of the two surfaces is sufficiently aggressive to cause localized surface contact during some time steps. Work is now in progress to develop the model to allow a boundary lubrication treatment to be substituted locally where such asperity collisions take place while maintaining the essential mass-conserving properties of the model.

The sensitivity to mesh size of the numerical results obtained with the model described in this paper is illustrated in Fig. 15. The film thickness calculated at two positions during transit of the contact area is illustrated for three different mesh sizes: $b/384$, $b/192$ and $b/96$. The results for these individual models are shown offset by 2, 3 and 4 μm respectively in the region of the figure where the film thickness is negative. The curves are also shown with no offset at the top of the figure. It is clear that there are no significant differences in the predicted film thickness as

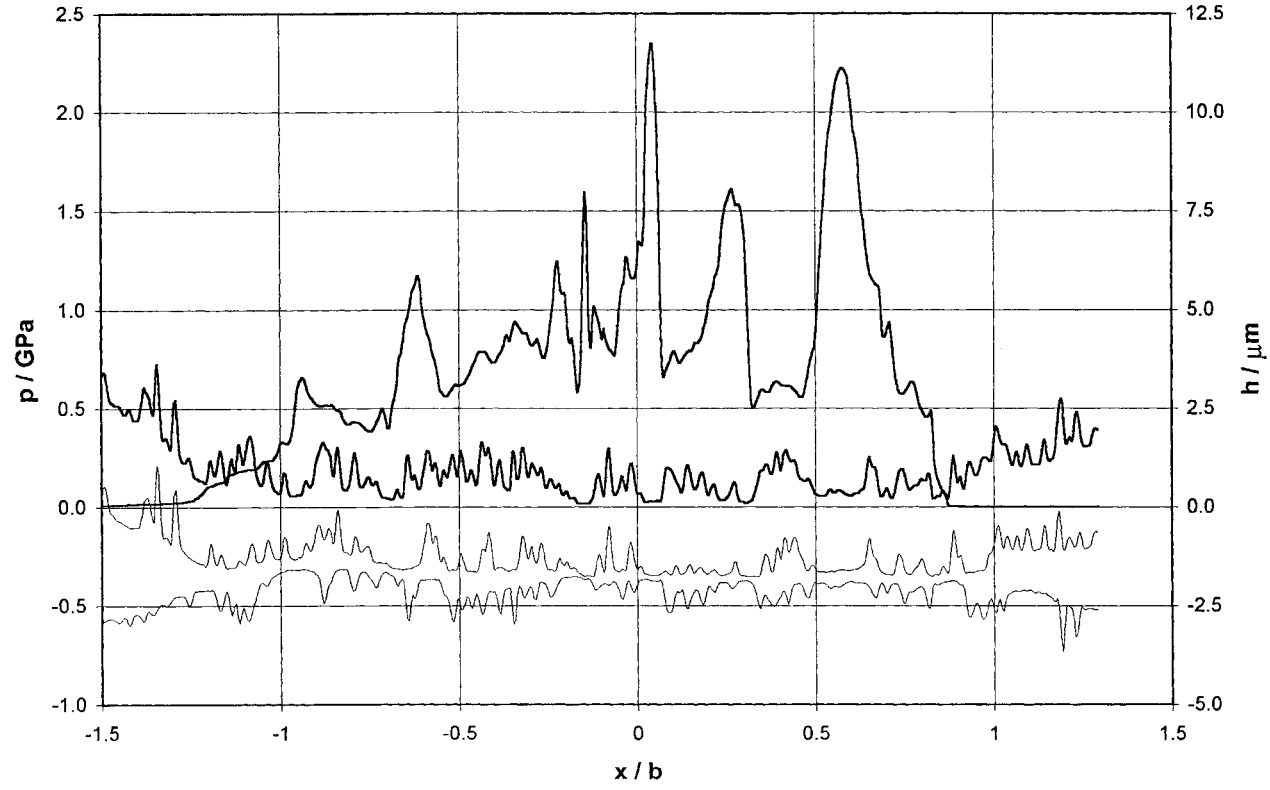

Fig. 12 Pressure (upper curve) and film thickness distributions at time step 4500 for $\bar{\xi} = -0.3$ and $U = 25$ m/s. Also shown (light curve) are the two rough surfaces at this time step in their contact configuration with a negative offset for clarity

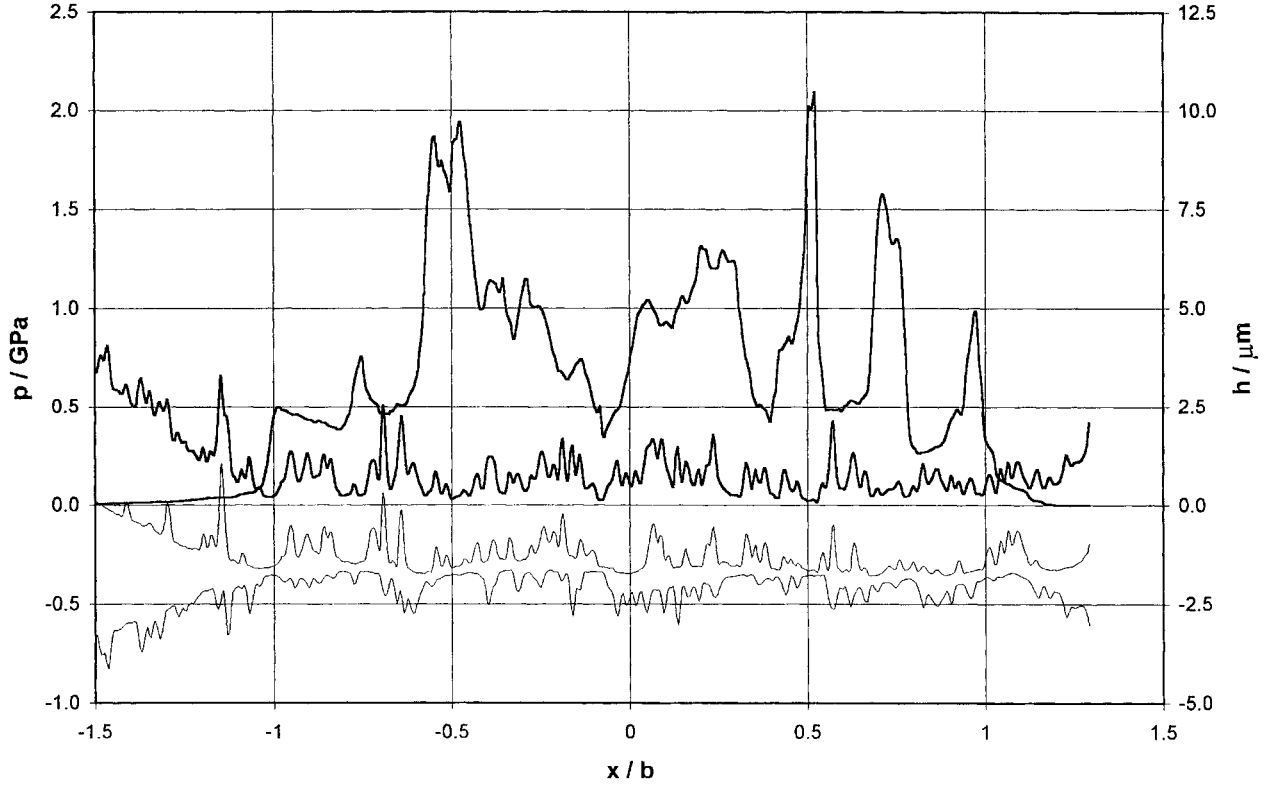

Fig. 13 Pressure (upper curve) and film thickness distributions at time step 5000 for $\bar{\xi} = -0.3$ and $U = 25$ m/s. Also shown (light curve) are the two rough surfaces at this time step in their contact configuration with a negative offset for clarity

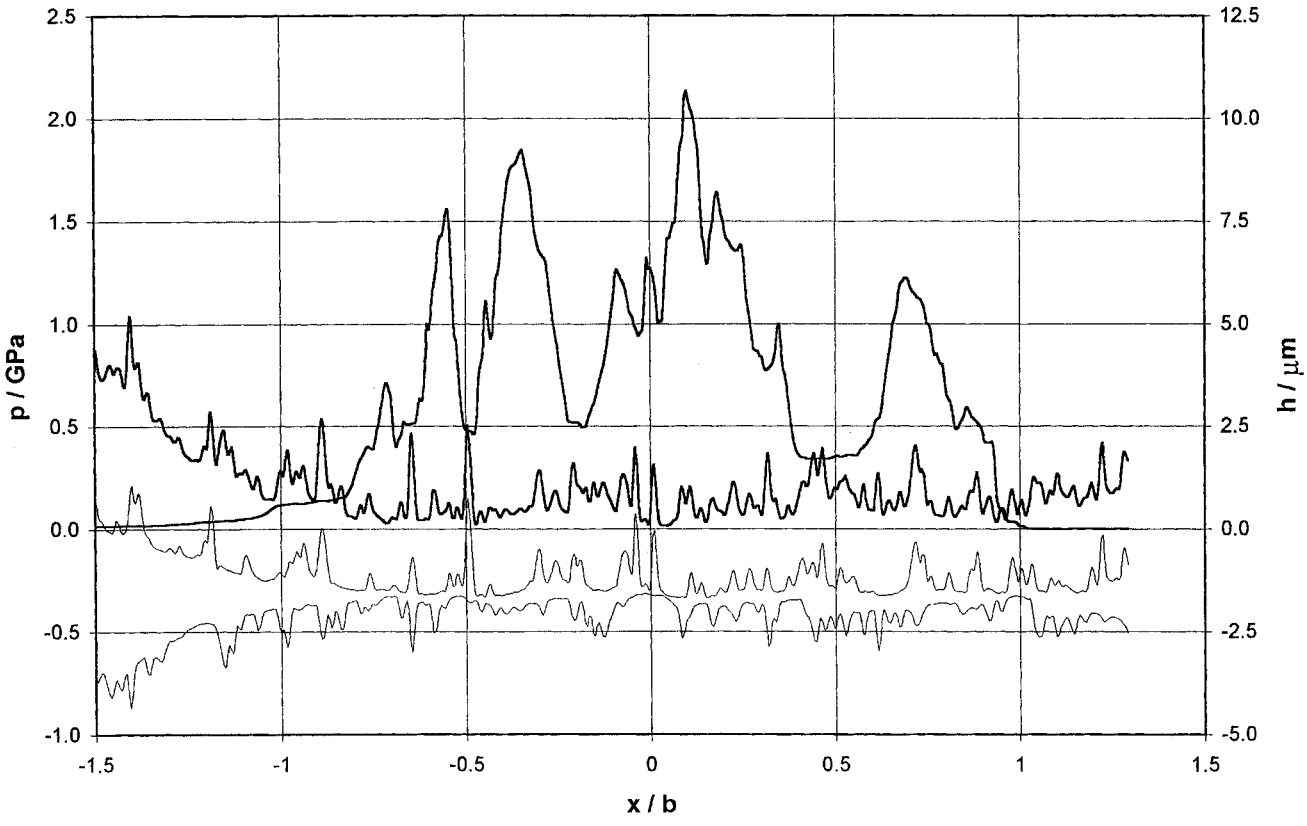

Fig. 14 Pressure (upper curve) and film thickness distributions at time step 5500 for $\xi = -0.3$ and $U = 25$ m/s. Also shown (light curve) are the two rough surfaces at this time step in their contact configuration with a negative offset for clarity

the mesh is varied; indeed detailed comparison of the results for $b/192$ and $b/384$ show that these film thickness curves are almost identical. There are minor shape differences at the asperity tips when the coarsest model is used, but this is an inevitable consequence of the reduced definition in the asperity geometry.

6 CONCLUSIONS

The new solution technique described in this paper enables highly stable time-dependent EHL solutions to be computed sufficiently quickly to allow examination of the behaviour of real gear lubrication conditions in which surface roughness is at least an order of magnitude greater than the minimum oil-film thickness. The crucial advantage of the coupled approach in dealing with these severe cases lies in the fact that film thickness and pressure are treated as simultaneously active variables throughout the solution process. This leads to a highly robust and rapidly convergent numerical scheme. A straightforward implementation of this approach causes the well-known difficulty of a fully populated solution matrix, however, which presents an overwhelming computing problem even for steady state, line contacts and virtually rules out time-dependent and two-dimensional cases. Partial coupling of deformation and pressure is found to be inadequate [**26**]. A key step in overcoming this obstacle is to formulate the elastic deformation in terms of its second differential which then allows the influence of distant points to be safely linearized (giving a solution matrix banded about its diagonal) without sacrificing any of the advantages of full coupling. The resulting coupled–iterative scheme is rapidly convergent and highly robust.

The results shown here demonstrate the ability of the method to handle severe cases of rough surfaces and thin films under time-varying conditions. A surprising feature of the results is that the pressure deviations developed are generally seen to have a wavelength that is longer than that of the smallest scale of roughness features. Indeed those features would seem to be of peripheral importance in determining lubricant pressure response except in the special case of pure rolling where the pressure becomes more sensitive to the finer scale asperities.

What are effectively asperity contacts have been observed in the case of two rough surfaces rolling/sliding together under severe conditions. Modelling of this real 'mixed lubrication' regime represents a significant challenge. The coupled method described in the paper lends

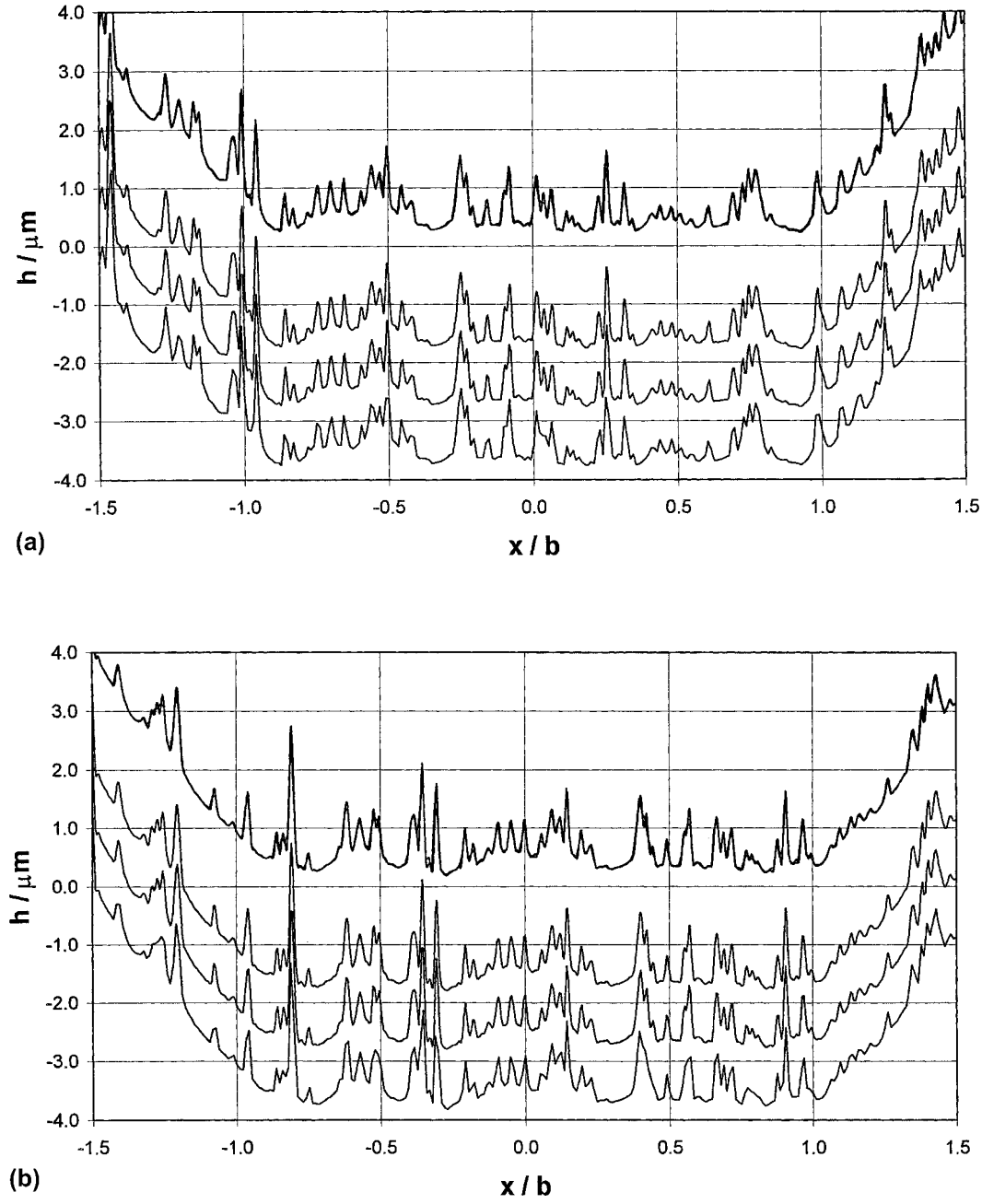

Fig. 15 Film thicknesses calculated at two positions, as shown in (a) and (b), during transit of the contact area using different mesh sizes. Curves are for $\delta x = b/384$ offset by -2 μm, for $\delta x = b/192$ offset by -3 μm and for $\delta x = b/96$ offset by -4 μm. Curves with no offset are superimposed at the top of figures

itself well to the inclusion of localized 'dry' or boundary lubricated regions. These may be determined dynamically within the overall EHL contact, since boundary conditions of zero film thickness can be imposed on the solution where required while maintaining the essential mass-conserving feature of the model.

Identifying suitable parameters to be obtained from EHL analyses of rough surfaces is another important development that is required if contact modelling is to produce useful information to quantify surface performance. It is possible to speculate that parameters that measure:

(a) pressure deviation from the mean,
(b) bearing ratio under EHL operation and
(c) load cycles per contact passage for load bearing asperities

may be found relevant in quantifying surface durability. Analyses in progress of surfaces produced by different

manufacturing methods incorporating a thermal treatment are providing data that allow development of such parameters.

This paper is concerned with line contacts, but the methods described are equally extendable to side-leakage point contacts and this work is now being pursued [**30**].

ACKNOWLEDGEMENTS

The authors acknowledge support of this work by the Engineering and Physical Sciences Research Council (Grant GR/L90996) and the British Gear Association. They are also grateful to Dr J. Tao for assitance in producing Fig. 15.

REFERENCES

1 **Grubin, A. N.** Fundamentals of the hydrodynamic theory of lubrication of heavily loaded cylindrical surfaces. Book 30, 1949 (Central Scientific Research Institute for Technology and Engineering, Moscow) (DSIR Translation 337).

2 **Dowson, D.** and **Higginson, G. R.** *Elastohydrodynamic Lubrication*, 1966 (Pergamon, Oxford).

3 **Bair, S.** and **Winer, W. O.** A rheological model for elastohydrodynamic contacts based on primary laboratory data. *Trans. ASME, J. Lubric. Technol.*, 1979, **101**, 258–265.

4 **Johnson, K. L.** and **Tevaarwerk, J. L.** The shear behaviour of elastohydrodynamic oil films. *Proc. R. Soc. Lond. A*, 1977, **356**, 215–236.

5 **Goglia, P. R., Cusano, C.** and **Conry, T. F.** The effects of surface irregularities on the elastohydrodynamic lubrication of sliding line contacts. Part I: single irregularities; Part II: wavy surfaces. *Trans. ASME, J. Tribology*, 1984, **106**, 104–112, 113–119.

6 **Lubrecht, A. A., Ten Napel, W. E.** and **Bosma, R.** The influence of longitudinal and transverse roughness on the elastohydrodynamic lubrication of circular contacts. *Trans. ASME, J. Tribology*, 1988, **110**, 421–426.

7 **Kweh, C. C., Evans, H. P.** and **Snidle, R. W.** Micro-elastohydrodynamic lubrication of an elliptical contact with transverse and three-dimensional sinusoidal roughness. *Trans. ASME, J. Tribology*, 1989, **111**, 577–584.

8 **Kweh, C. C., Patching, M. J., Evans, H. P.** and **Snidle, R. W.** Simulation of elastohydrodynamic contacts between rough surfaces. *Trans. ASME, J. Tribology*, 1992, **114**, 412–419.

9 **Chang, L.** and **Webster, M. N.** A study of elastohydrodynamic lubrication of rough surfaces. *Trans. ASME, J. Tribology*, 1991, **113**, 110–115.

10 **Venner, C. H.** and **Lubrecht, A. A.** Transient analysis of surface features in an EHL line contact in the case of sliding. *Trans. ASME, J. Tribology*, 1994, **116**, 186–193.

11 **Greenwood, J. A.** and **Morales-Espejel, G. E.** The behaviour of transverse roughness in EHL contacts. *Proc. Instn Mech. Engrs, Part J, Journal of Engineering Tribology*, 1994, **208**(J2), 121–132.

12 **Chang, L., Webster, M. N.** and **Jackson, A.** On the pressure rippling and roughness deformation in elastohydrodynamic lubrication of rough surfaces. *Trans. ASME, J. Tribology*, 1993, **115**, 439–444.

13 **Chang, L.** and **Zhao, W.** Fundamental differences between Newtonian and non-Newtonian micro-EHL results. *Trans. ASME, J. Tribology*, 1995, **117**, 29–35.

14 **Venner, C. H.** and **Ten Napel, W. E.** Surface roughness effects in an EHL line contact. *Trans ASME, J. Tribology*, 1992, **114**, 616–622.

15 **Ai, X.** and **Cheng, H. S.** A transient EHL analysis for line contacts with measured surface roughness using multigrid technique. *Trans. ASME, J. Tribology*, 1994, **116**, 549–556.

16 **Venner, C. H.** and **Lubrecht, A. A.** Numerical analysis of the influence of waviness on the film thickness of a circular EHL contact. *Trans. ASME, J. Tribology*, 1996, **118**, 153–161.

17 **Xu, G.** and **Sadeghi, F.** Thermal EHL analysis of circular contacts with measured surface roughness. *Trans. ASME, J. Tribology*, 1995, **117**, 473–483.

18 **Okamura, H.** A contribution to the numerical analysis of isothermal elastohydrodynamic lubrication. In *Tribology of Reciprocating Engines*, Proceedings of the 9th Leeds–Lyon Symposium on *Tribology*, Leeds, 1982, 1983, pp. 313–320 (Butterworth, London).

19 **Houpert, L. G.** and **Hamrock, B. J.** Fast approach for calculating film thicknesses and pressures in elastohydrodynamically lubricated contacts at high loads. *Trans. ASME, J. Tribology*, 1986, **108**, 411–420.

20 **Evans, H. P.** and **Hughes, T. G.** Evaluation of deflection in semi-infinite bodies by a differential method. *Proc. Instn Mech. Engrs, Part C, Journal of Mechanical Engineering Science*, 2000, **214**(C4), 563–584.

21 **Hughes, T. G., Elcoate, C. D.** and **Evans, H. P.** Coupled solution of the elastohydrodynamic line contact problem using a differential deflection method. *Proc. Instn Mech. Engrs, Part C, Journal of Mechanical Engineering Science*, 2000, **214**(C4), 585–598.

22 **Conry, T. F., Wang, S.** and **Cusano, C.** A Reynolds–Eyring equation for elastohydrodynamic lubrication in line contacts. *Trans. ASME, J. Tribology*, 1987, **109**, 648–654.

23 **Sharif, K. J., Morris, S. J., Evans, H. P.** and **Snidle, R. W.** Comparison of non-Newtonian EHL models in high sliding applications. In Proceedings of the 27th Leeds–Lyon Symposium on *Tribology*, Lyon, 2000, 2001 (Elsevier, Amsterdam).

24 **Roelands, C. J. A.** Correlational aspects of the viscosity–temperature–pressure relationship of lubricating oils. Druk. URB, Grönigen, 1966.

25 **Hughes, T. G., Elcoate, C. D.** and **Evans, H. P.** A novel method for integrating first and second order differential equations in elastohydrodynamic lubrication for the solution of smooth isothermal, line contact problems. *Int. J. Numer. Meth. Engng*, 1999, **44**, 1099–1113.

26 **Elcoate, C. D.** Coupled solution methods for the elastohydrodynamic problem. PhD thesis, University of Wales, 1996.

27 **Britton, R. D., Elcoate, C. D., Alanou, M. P., Evans, H. P.** and **Snidle, R. W.** Effect of surface finish on gear tooth friction. *Trans. ASME, J. Tribology*, 2000, **122**, 354–360.

28 **Patching, M. J.** The effect of surface roughness on the micro-elastohydrodynamic lubrication and scuffing performance of aerospace gear tooth contacts. PhD thesis, University of Wales, 1994.

29 **Elcoate, C. D., Evans, H. P., Hughes, T. G.** and **Snidle, R. W.** Fully coupled elastohydrodynamic solution techniques for the analysis of real rough line contacts using finite element

and finite difference models. In *Lubrication at the Frontier*, Proceedings of the 25th Leeds–Lyon Symposium on *Tribology*, Lyon, 1998, 1999, pp. 163–174 (Elsevier, Amsterdam).

30 Holmes, M. A fully coupled method for solving the Newtonian steady state isothermal elastohydrodynamic point contact problem. *Proc. South Wales Inst. Engrs*, 2000, **108**.

APPENDIX

The averaged terms in equation (13) are evaluated over the element as follows:

$$\tilde{\rho} = \sum_{k=1}^{n_n} N_k \rho_k, \qquad \tilde{h} = \sum_{k=1}^{n_n} N_k h_k, \qquad \tilde{\eta} = \sum_{k=1}^{n_n} N_k \eta_k$$

$$\frac{\partial \tilde{\rho}}{\partial x} = \sum_{k=1}^{n_n} \frac{\partial N_k}{\partial x} \rho_k, \qquad \frac{\partial \tilde{p}}{\partial x} = \sum_{k=1}^{n_n} \frac{\partial N_k}{\partial x} p_k$$

$$\frac{\partial \tilde{h}}{\partial x} = \sum_{k=1}^{n_n} \frac{\partial N_k}{\partial x} h_k$$

$$\tilde{h}^3 = (\tilde{h})^3, \qquad \tilde{S} = S\left(\tilde{\eta},\ \tilde{h},\ \frac{\partial \tilde{p}}{\partial x}\right) \tag{14}$$

Hydrodynamic equation submatrix entries are

$$\mathbf{R}_p = (1-\theta)\,\Delta t \left(\frac{1}{12}\int \frac{\partial N_i}{\partial x}\frac{\tilde{\rho}\tilde{h}^3}{\tilde{\eta}}\tilde{S}\frac{\partial N_j}{\partial x}\,\mathrm{d}x\right)\Bigg|^{t+\Delta t} \tag{15}$$

$$\mathbf{R}_h = (1-\theta)U\,\Delta t \int N_i\left(\frac{\partial \tilde{\rho}}{\partial x}N_j + \tilde{\rho}\frac{\partial N_j}{\partial x}\right)\mathrm{d}x + \int N_i \tilde{\rho} N_j\,\mathrm{d}x\Bigg|^{t+\Delta t} \tag{16}$$

$$\mathbf{R}_r = \int N_i \tilde{\rho}\tilde{h}\,\mathrm{d}x - \theta\,\Delta t\left[U\int N_i\left(\tilde{h}\frac{\partial \tilde{\rho}}{\partial x} + \tilde{\rho}\frac{\partial \tilde{h}}{\partial x}\right)\mathrm{d}x + \frac{1}{12}\int \frac{\partial N_i}{\partial x}\frac{\tilde{\rho}\tilde{h}^3}{\tilde{\eta}}\frac{\partial \tilde{p}}{\partial x}\tilde{S}\,\mathrm{d}x\right]\Bigg|^{t} \tag{17}$$

where Gauss point integration is used to evaluate the integrals over each finite element.

Elastic equation submatrix entries are

$$\mathbf{E}_h = \begin{cases} 1 & \text{for } j = i \\ -0.5 & \text{for } j = i \pm 1 \\ 0 & \text{elsewhere} \end{cases} \tag{18}$$

$$\mathbf{E}_p = \begin{cases} \dfrac{\Delta^2}{2} f_{j-i} & \forall |j-i| \leqslant K \\ 0 & \text{elsewhere} \end{cases} \tag{19}$$

$$\mathbf{E}_r = -\frac{\Delta^2}{2}\sum_{|k-i|>K} f_{k-i}\,p_k - \frac{\Delta^2}{2R} + \varphi_i - \frac{\varphi_{i+1}+\varphi_{i-1}}{2} \tag{20}$$

The boundary conditions are applied as follows. At $i = 1$ and at $i = n$ the pressure is set to zero. At $i = 1$ the film thickness is set to a prescribed value, so that h_1 has an equivalent role to the constant h_s in equation (5). The value of h_1 is specified in order to obtain the required load. The contributions for the elastic equation at $i = 1$ are

$$\mathbf{E}_h = \begin{cases} 1 & \text{for } j = i \\ 0 & \text{for } j \neq i \end{cases}$$

$$\mathbf{E}_p = 0, \qquad \mathbf{E}_r = h_1$$

At $i = n$ the film thickness h_n is obtained by using equations (5) and (7) to evaluate the difference $h_n - h_1$ to give

$$h_n - h_1 + \sum_{\text{all } k}(g_{k-1} - g_{k-n})p_k = \frac{x_n^2 - x_1^2}{2R} + \varphi(x_n,\ t) - \varphi(x_1,\ t)$$

so that in equation (13) at $i = n$

$$\mathbf{E}_h = \begin{cases} 1 & \text{for } j = i \\ -1 & \text{for } j = 1 \\ 0 & \text{elsewhere} \end{cases}$$

$$\mathbf{E}_p = g_{j-1} - g_{j-n}$$

$$\mathbf{E}_r = \frac{x_n^2 - x_1^2}{2R} + \varphi(x_n,\ t) - \varphi(x_1,\ t)$$

As the $\mathbf{E}_p$ terms are all significant for this last elastic equation they are all included in the left-hand side of equation (13). This row has to be eliminated numerically during the solution process but this does not present an impediment to the rapid solution of the equation.